



Size-dependent gold nanoparticles induce macrophage M2 polarization and promote intracellular clearance of *Staphylococcus aureus* to alleviate tissue infection



Wang Peilin^{a,1}, Peng Ying^{a,1}, Wang Renyuan^{a,1}, Li Zhuoxuan^a, Yang Zhenwu^a, Zhao Mai^a, Song Jianguo^a, Zhang Hao^a, Yin Gang^a, Lin Lin^{b,**}, Lin Haodong^{a,*}

^a Trauma Center, Shanghai General Hospital, Shanghai Jiao Tong University School of Medicine, Shanghai 201620, China

^b School of Chemical and Environmental, Engineering, Shanghai Institute of Technology, Shanghai 201418, China

ARTICLE INFO

Keywords:

Au nanoparticles
Osteomyelitis
Wound infection
Staphylococcus aureus
Macrophages polarization
Phagocytosis
Autophagy

ABSTRACT

Tissue infection typically results from blood transmission or the direct inoculation of bacteria following trauma. The pathogen-induced destruction of tissue prevents antibiotics from penetrating the infected site, and severe inflammation further impairs the efficacy of conventional treatment. The current study describes the size-dependent induction of macrophage polarization using gold nanoparticles. Gold nanoparticles with a diameter of 50 nm (Au50) can induce M2 polarization in macrophages by inhibiting the NF- κ B signaling pathway and stimulate an inflammatory response in the environment by inhibiting the MAPK signaling pathway LPS. Furthermore, the induced polarization and anti-inflammatory effects of the Au50 nanoparticles promoted the osteogenic differentiation of BMSCs in vitro. In addition, the overexpression of TREM2 in macrophage induced by Au50 nanoparticles was found to promote macrophage phagocytosis of *Staphylococcus aureus*, enhance the fusion of autophagosomes and lysosomes, accelerate the intracellular degradation of *S. aureus*, in addition to achieving an effective local treatment of osteomyelitis and infectious skin defects in conjunction with inflammatory regulation and accelerating bone regeneration. The findings, therefore, demonstrate that Au50 nanoparticles can be utilized as a promising nanomaterial for in vivo treatment of infections.

1. Introduction

Staphylococcus aureus (*S. aureus*) is one of the most common bacteria causing tissue infection, which is frequently caused by the invasion of suppurative microorganisms in trauma [1,2]. The clinical incidence rate of common tissue infections, such as osteomyelitis, is 1–13 per 100,000 people, and the incidence rate of osteomyelitis in long bones or open fractures is 4%–64% [3,4], whereas wound infection is the most common tissue infection caused by trauma and the main complication of surgery [5,6]. Due to numerous factors, including the low bioavailability of antibiotics, the ineffective sterilization of phagocytes, and the destruction of infection tissue, determining the optimal treatment strategy for osteomyelitis and wound infection remains difficult despite the rapid

development of medical science. In the case of osteomyelitis, severe and persistent inflammation plays a crucial role in preventing osteogenesis. At the site of infection, pathogens can produce bacterial toxins that severely damage blood vessels and bone tissue, preventing antibiotics from penetrating the infected area and accelerating bone destruction [7]. In recent years, various materials used in the treatment of osteomyelitis have achieved satisfactory results [8,9], but there are still some deficiencies, such as secondary injury of material removal, metabolic toxicity of material in vivo, and its specific molecular mechanism is unknown. Nanoparticles are designed as nanoscale (1–100 nm) synthetic building blocks for drug delivery, construct scaffold to fill the repair promoting factor and other medical applications [10,11]. It has been shown that nanoparticles interact with biological organisms to produce

* Corresponding author.

** Corresponding author.

E-mail addresses: palinwang@126.com (W. Peilin), 13122177028@163.com (P. Ying), Willowrenyuan@hotmail.com (W. Renyuan), 342601440@qq.com (L. Zhuoxuan), 894546983@qq.com (Y. Zhenwu), zhao_mai@outlook.com (Z. Mai), 3048029476@qq.com (S. Jianguo), zhanghao_673@163.com (Z. Hao), yingangz@163.com (Y. Gang), linlin@sit.edu.cn (L. Lin), haodonglin@hotmail.com (L. Haodong).

¹ These authors contributed equally to this work.

<https://doi.org/10.1016/j.mtbio.2023.100700>

Received 8 February 2023; Received in revised form 19 May 2023; Accepted 29 May 2023

Available online 20 June 2023

2590-0064/© 2023 The Author(s). Published by Elsevier Ltd. This is an open access article under the CC BY-NC-ND license (<http://creativecommons.org/licenses/by-nc-nd/4.0/>).

specific biological effects and activate the innate immune system [12–14]. However, the effects of nanoparticles of various diameters on cells are quite distinct. According to reports, inflammation induced by nanoparticles can result in toxicity such as tissue fibrosis or allergy [15, 16]. However, depending on the physical and chemical properties of nanoparticles, this reaction can also enhance the cellular and humoral immune response against infection or tumor [17–19]. To promote clinical application, the optimal materials for a potential osteomyelitis treatment should adhere to a set of standards. Local treatment with a minimally invasive strategy, for instance, can alleviate the pain of patients by reducing systemic toxicity and achieve effective bacterial inhibition at the site of infection [20]. In addition, materials that can promote tissue repair are preferable in the treatment of tissue infection, such as treatment of osteomyelitis with osteogenic materials, which is typically accompanied by bone degeneration [21,22]. However, promoting tissue regeneration while simultaneously eliminating bacteria remains a formidable challenge.

As the first line of defense for innate immunity against bacterial invaders, macrophages have the unique function of “swallowing” various foreign bodies in the human body, preserving normal macrophage function, and effectively eliminating bacteria from the human body [23]. When macrophages consume bacteria, phagosomes envelop bacteria and fuse with lysosomes. In the phagolysosome body, bacteria are digested by enzymes and other toxic peroxidases, and the destroyed bacteria are then expelled as soluble fragments [24]. In addition to eliminating bacteria, macrophages can secrete repair-promoting cytokines via M2 polarization, thereby accelerating tissue regeneration and promoting wound healing [25]. Autophagy is a cellular process, which engulfs proteins, lipids, and organelles into autophagosomes, and targets lysosomes for fusion and degradation. However, it has also been proved to be able to resist the infection of a variety of pathogenic bacteria [26]. In response, bacteria have developed numerous strategies to avoid autophagy by interfering with autophagy signals or mechanisms. In some cases, they use autophagy to stimulate their own growth [27]. *S. aureus* has been demonstrated to stay in autophagosomes of macrophages, inhibit lysosomal fusion, and incubate continuously [28]. Notably, nanoparticles roughly the same size as invading microorganisms and autologous components have been proved to induce autophagy via endocytosis/phagocytosis-dependent mechanisms, oxidative stress, or mTOR-dependent pathways [29–32]. However, how autophagy regulates bacterial intracellular clearance in response to stimulation by nanomaterials with distinct physical and chemical properties remains to be determined.

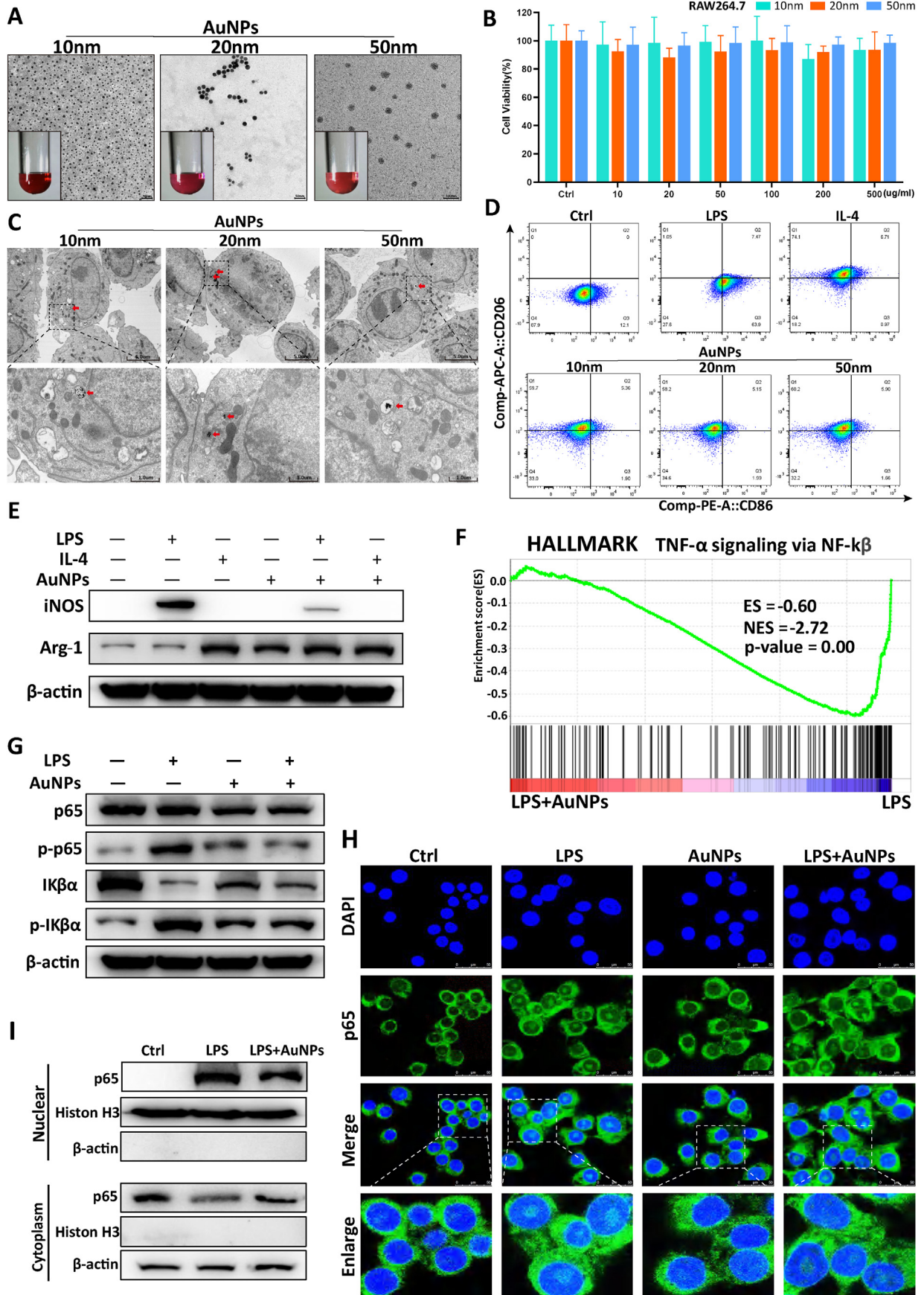
In this research, we investigated the effects of gold nanoparticles on macrophage cells to eliminate *S. aureus* and induce polarization, as well as the molecular mechanism underlying these effects using high-throughput transcriptome analysis. Our research demonstrates that Au50 can induce M2 polarization of macrophages to inhibit inflammatory responses, which may be accomplished by inhibiting NF- κ B and MAPK signaling pathways and ultimately promoting tissue repair. In addition, we demonstrated that 50 nm gold nanoparticles overexpressing TREM2 promotes macrophage phagocytosis of *S. aureus* and induce VAMP8 to interact with STX17 and SNAP29 to promote the fusion of autophagosomes and lysosomes, enhance the autophagy process, and accelerate intracellular bacterial degradation. Consequently, we discovered that Au50 nanoparticles have a previously unidentified function and mechanism in the intracellular sterilization and polarization reaction of macrophages, which can aid the body in antibacterial and tissue repair. Furthermore, these findings provide new horizon and scientific basis for the development of effective antibacterial anti-inflammatory immunotherapy utilizing nanoparticles.

2. Result

2.1. Size-dependent M2 polarization in macrophages were induced by Au50 inhibiting the NF- κ B signaling pathway

To gain insight into the specific function of engineered nanoparticles in macrophages, we first synthesized gold nanoparticles (AuNPs) with average diameters of 10, 20, and 50 nm, and conducted mechanistic studies by transmission electron microscopy (TEM) (Fig. 1A). The hydrodynamic size distribution, polydispersity index, zeta potential and endotoxin content of Au nanoparticles in a DMEM medium were investigated (Figure S1A). The cytotoxicity of gold nanoparticles at various concentrations was found to be extremely low when tested on RAW264.7 cells (Fig. 1B) and BMDMs (Figure S1B). Consequently, we selected 200 μ g/mL as the experimental concentration of Au nanoparticles for subsequent experiments. Subsequently, we added AuNPs (200 μ g/mL) and LPS (100 ng/mL) to the culture medium for 24 h and tested the endotoxin levels in their supernatant (Figure S1C) and sediment (Figure S1D). The results showed that AuNPs were unable to adsorb LPS. Using TEM, we observed that different-sized Au nanoparticles can be ingested by RAW264.7 cells (Fig. 1C) and BMDMs (Figure S1E), allowing them to exert further influence on cells. In order to induce M1 and M2 polarization of macrophages, we initially primed RAW264.7 cells with lipopolysaccharide (LPS) and interleukin 4 (IL-4). Subsequently, western blot and flow cytometry were used to detect the polarization induction of RAW264.7 cells by Au nanoparticles of varying diameters. In flow cytometry (Fig. 1D), CD86 was utilized as an M1 polarization marker and CD206 as an M2 polarization marker of macrophages, whereas in western blot, iNOS and CD86 were utilized as M1 polarization markers and Arg-1 and CD206 was utilized as M2 polarization markers (Figure S2A). In addition, the RT-PCR was used to measure the mRNA expression of M1 and M2 polarization markers and cytokines in response to the same treatment (Figure S2B). The preceding results demonstrate that Au nanoparticles with three different diameters can induce M2 polarization in macrophages, particularly Au50. To confirm the effects of Au50 nanoparticles in macrophages polarization, we combined Au50 with LPS and IL-4 individually or in pairs to induce the polarization of RAW264.7 cells (Fig. 1E) and BMDMs (Figure S2C), and estimated the expression level of polarized labeled proteins. Even in the presence of LPS stimulation, Au50 was found to induce macrophage M2 polarization. In addition, the cause of Au50 nanoparticle-induced M2 polarization of macrophages was investigated. RAW264.7 cells were induced for 48 h after LPS stimulation for 6 h, and RNA-seq analysis was used to investigate the underlying mechanism of Au50 nanoparticles-induced effects. Moreover, the GSEA analysis was then used to uncover the underlying mechanisms of M2 polarization of macrophages induced by Au50, and the results indicated that the TNF- α signaling via the NF- κ B signaling pathway of HALLMARK was significantly enriched in cluster LPS (Fig. 1F). This is consistent with previous findings that inhibiting the NF- κ B signaling pathway promotes macrophage M2 polarization [33–35].

In addition, the results of the bioinformatics analysis were validated through molecular biology. The expression level of NF- κ B signaling pathway proteins was analyzed using western blotting after stimulated by Au50 and LPS individually or in pairs (Fig. 1G). Immunofluorescence (Fig. 1H) and nucleoprotein separation experiments (Fig. 1I) confirmed that Au50 inhibited the nuclear translocation induced by LPS of the p65 protein. The result showed that Au50 was able to inhibit the activation of the NF- κ B signaling pathway induced by LPS. Additionally, we confirmed the inhibition of Au50 on the NF- κ B signaling pathway using a time- and concentration-dependent gradient (Figure S2D). In addition, inhibitors (JSH-23, JSH) and activators (Betulinic acid, BetA) of the NF- κ B signaling pathway, along with LPS and Au50, induced the polarization of macrophage cells (Figure S2E). Activation of the NF- κ B pathway was unable to induce M1 polarization, while inhibition of the NF- κ B pathway was unable to induce M2 polarization.



(caption on next page)

Fig. 1. Size-dependent M2 polarization in macrophages was induced by Au50 inhibiting the NF- κ B signaling pathway. (A) Optical images of Au nanoparticle suspension and TEM analysis of Au nanoparticles. The scale bar presents as indicated. (B) Toxicity of Au nanoparticles with different concentrations (10, 20, 50, 100, 200, 500 μ g/mL) on RAW264.7 cells. (C) TEM analysis for the intracellular locations of Au nanoparticles in RAW264.7 cells incubated with 200 μ g/mL Au nanoparticles for 48 h. The red arrows indicate nanoparticles. (D) Co-expression of CD86 and CD206 in RAW264.7 cells after LPS (100 ng/mL, 6 h), IL-4 (20 ng/mL, 24 h), and Au nanoparticles (200 μ g/mL, 48 h) treatment. Flow cytometry for M1 and M2, using CD86 as M1 mark, and using CD206 as M2 mark. (E) Immunoblot analysis the expression of iNOS and Arg-1 of cell lysates of RAW264.7 cells primed with LPS (100 ng/mL, 6 h), IL-4 (20 ng/mL, 24 h), and Au50 nanoparticles (200 μ g/mL, 48 h) treatment. (F) GSEA enrichment plots showing significantly enriched the downregulated signaling pathways of the TNF- α signaling via NF- κ B of HALLMARK. (G) LPS (100 ng/mL, 6 h) and Au50 nanoparticles (200 μ g/mL, 48 h) stimulate RAW264.7 cells respectively or in pairs. The expression levels of related proteins in the NF- κ B signaling pathway (I κ B α , p65, p-I κ B α and p-p65) were analyzed by western blot. (H) The phenomenon of p65 entering the nucleus by RAW264.7 cells was visualized and imaged under a confocal microscope. The green fluorescence showed that p65 was in the nucleus or cytoplasm after treatment. The nuclear staining was performed by DAPI. (I) The nuclear and cytoplasmic proteins were isolated and extracted, and their p65 protein levels were analyzed by Western blot. (For interpretation of the references to colour in this figure legend, the reader is referred to the Web version of this article.)

2.2. The inflammatory response induced by LPS in macrophages were attenuated by Au50 through the inhibition of MAPK signaling pathway

In the course of investigating the polarization of macrophages induced by Au50 nanoparticles, we discovered that macrophage inflammatory factors were not secreted in response to Au50 nanoparticle stimulation (Figure S2B and Fig. 2A). Accordingly, we explored the impact of nanoparticles on the secretion of inflammatory cytokines. The RT-PCR was used to detect the mRNA levels of inflammatory cytokines following stimulation of Au50 and LPS individually or in pairs (Fig. 2B). To further investigate the mechanism, a Gene Ontology (GO) enrichment analysis revealed that the term inflammatory response was the most distinguishing term between the two clusters (Fig. 2C). Moreover, the GSEA analysis was then used to uncover the underlying mechanisms of Au50-induced M2 polarization of macrophages, and the results indicated that the three downregulated pathways, including the Cytokine signaling pathway of REACTOME, the Inflammatory response of HALLMARK, and the MAPK signaling pathway of KEGG, were significantly enriched in cluster LPS (Fig. 2D). Therefore, we hypothesized that Au50 reduces the inflammatory factor secretion induced by LPS from inhibiting the MAPK signaling pathway. We clustered all the genes involved in the three GSEA pathways depicted in Fig. 2C and selected the top 50 genes based on the degree of differential expression to generate a heat map for gene clustering (Fig. 2E). The above RNA-seq enrichment analysis revealed that the genetic expression of the MAPK signaling pathway was significantly lower than that of the LPS cluster. Using a western blot, we determined that the phosphorylation of p38 and JNK induced by LPS was decreased, whereas the phosphorylation of ERK has no discernible change when stimulated by Au50 (Fig. 2F). In addition, we confirmed the inhibition of Au50 on the MAPK signaling pathway using a time- and concentration-dependent gradient (Figure S2F). Subsequently, we further investigated the relationship between MAPK and macrophage M2 polarization or NF- κ B. We use MAPK pathway activators (C16-PAF, C16) and inhibitors (Doramapimod, Drp) to induce macrophage polarization, either individually or in combination with LPS and Au50 (SFig. 2G). The result showed that activation of the MAPK pathway was unable to induce M1 polarization, while inhibition of the MAPK pathway was unable to induce M2 polarization. Subsequently, we validated the combined effect of NF- κ B and MAPK on the imaging of macrophage M2 polarization. We use MAPK and NF- κ B pathway activators (Gypenoside L, GpL) and inhibitors (Atracic acid, Atra) to induce macrophage polarization, either individually or in combination with LPS and Au50 (SFig. 2H). The result showed that although activation of the NF- κ B and MAPK pathway was unable to induce macrophage M1 polarization, inhibition of the NF- κ B and MAPK pathway was restricted the LPS-triggered M1 polarization and induced M2 polarization.

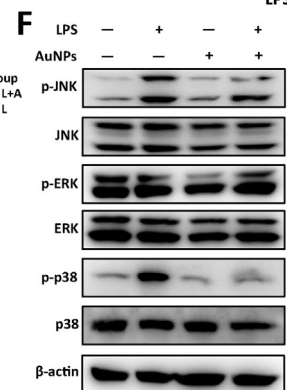
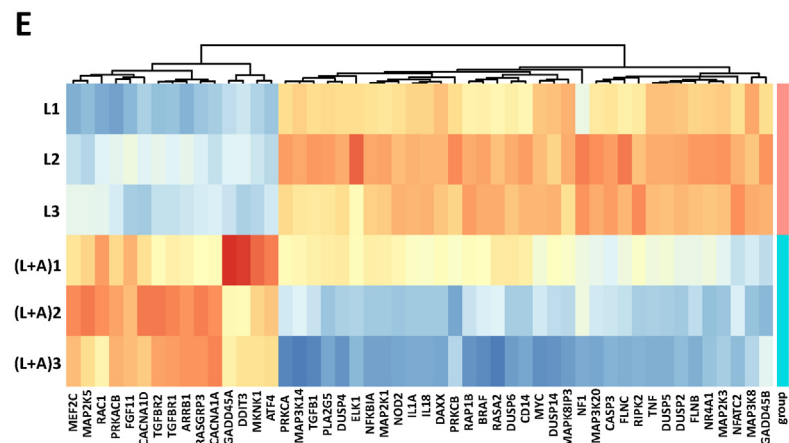
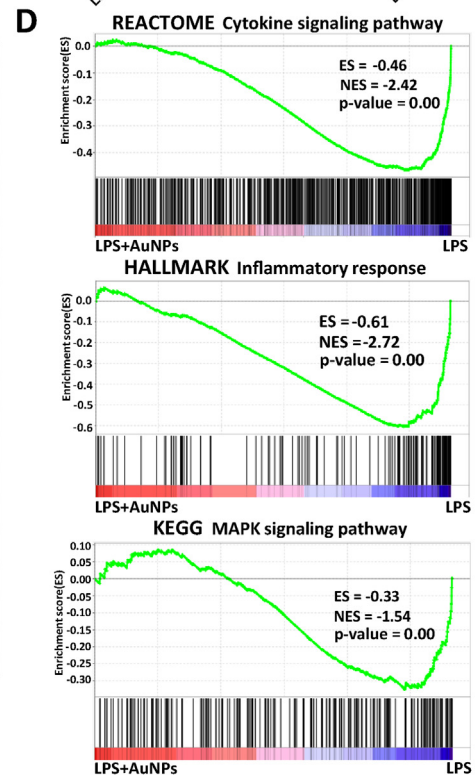
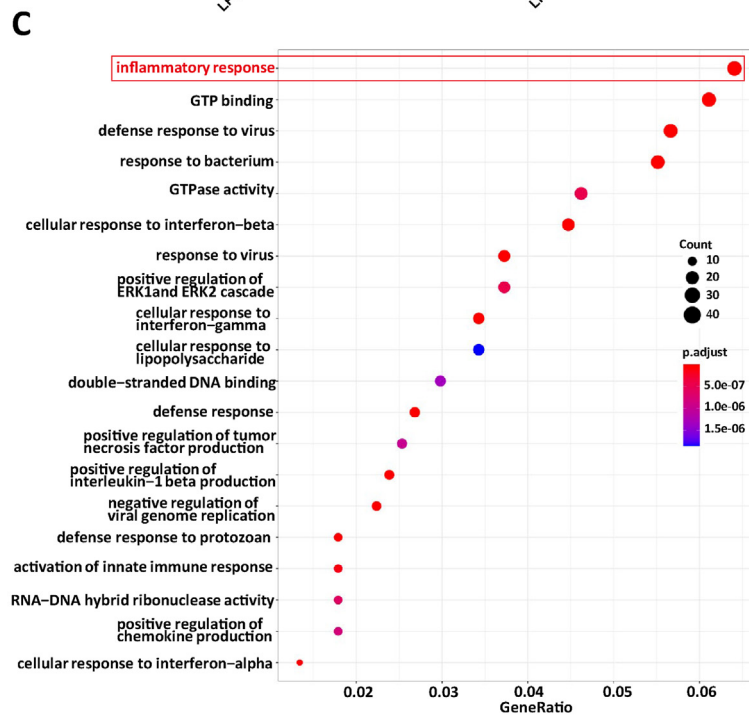
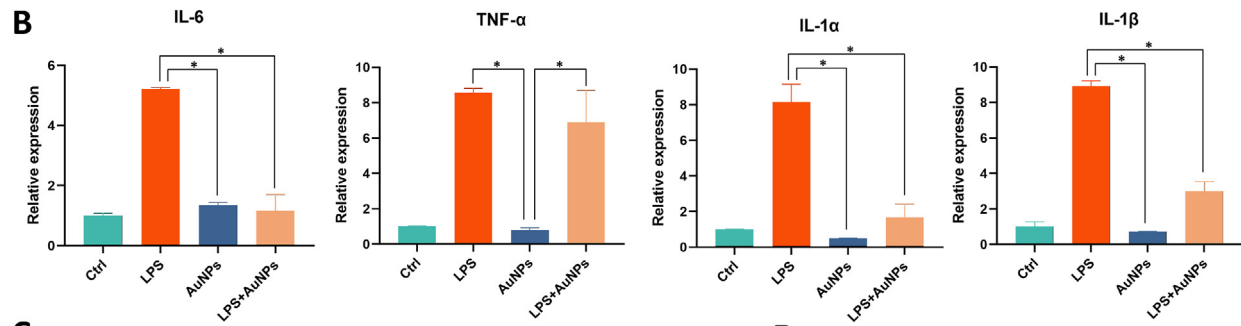
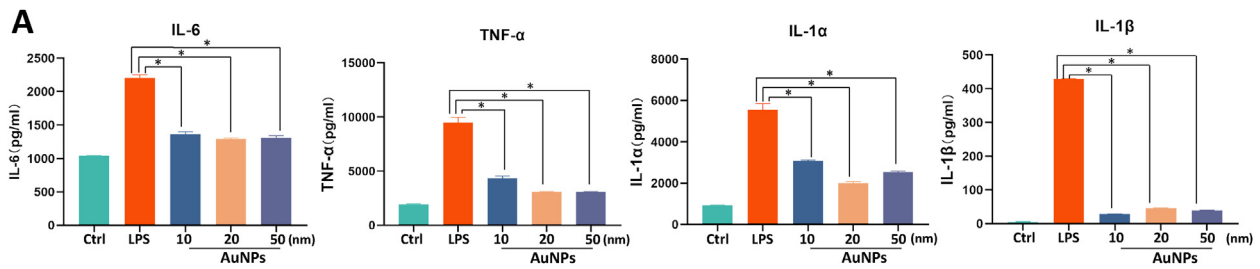
2.3. The osteogenesis differentiation of peripheral cells were promoted by Au50 reducing the secretion of inflammatory factors in macrophage

Our research has shown that Au50 nanoparticles can induce macrophages M2 polarization and suppress the secretion of inflammatory

cytokines. However, the living environment of macrophages was relatively complex, necessitating additional investigations to explore the effect of macrophages on peripheral cells stimulated by Au50 nanoparticles. We detected the osteogenic differentiation ability of BMSC after 7 or 14 days of Au50 stimulation using ALP staining. The results showed that there was no significant difference in the osteogenic differentiation ability of BMSC after 7 or 14 days of Au50 stimulation (Fig. 3A). Accordingly, we used bone marrow-derived macrophages (BMDMs) to create a conditioned medium (CM) to simulate the bone marrow microenvironment in order to observe the effects of macrophages stimulated by Au50 nanoparticles on osteoblastic differentiation of bone mesenchymal stem cells (BMSCs). The results demonstrated that alkaline phosphatase (ALP) staining (Fig. 3B) and alizarin red (AR) staining (Fig. 3C) confirmed that the osteogenic differentiation of BMSCs increased after treatment with CM-AuNPs and CM-LPS + AuNPs, compared to CM-LPS alone. In addition, the osteogenic differentiation protein level (Fig. 3D) and mRNA expression (Fig. 3E) of BMSCs increased following treatment with the CM of BMDMs stimulated by Au50 nanoparticles, even following treatment with the CM of BMDMs stimulated by both LPS and Au50 nanoparticles. Subsequently, we examined the secretion of EGFR and VEGFR that was simultaneously stimulated by ELISA (Fig. 3F) and RT-PCR (Fig. 3G) in response to the remarkable cytokines of vascular differentiation. No obvious discrepancy could be observed in the secretion of EGFR, although the expression level of mRNA increased. In addition, the secretion and mRNA expression level of VEGFR increased following treatment with CM-AuNPs and CM-LPS + AuNPs, when compared to treatment with CM-LPS. Therefore, this may be related to the promotion of peripheral cell angiogenic differentiation, which remains to be further explored.

2.4. The phagocytosis and intracellular sterilization of macrophages to *S. aureus* was promoted by Au50 induces overexpressing TREM2

Macrophages were the primary defense cells of the organism in response to foreign microbes and bacterial infections; however, our previous experiments demonstrated that the polarization state of macrophages could be altered and inflammatory responses could be suppressed by Au50 nanoparticles, which are also essential mechanisms for macrophages to deal with the external invasion [36]. Therefore, we infected macrophages that had been pretreated with Au50 nanoparticles with *S. aureus*, co-cultured the Au50 nanoparticles with *S. aureus*, and determined the extracellular and intracellular antibacterial effects of Au50 nanoparticles by bacterial plate count. Through bacterial plate counting, we tested the extracellular antibacterial activity of Au50 nanoparticles against *S. aureus* in broth (Figure S3A) and LB (Figure S3B) culture medium, as well as intracellular (Fig. 4A) antibacterial activity. The results of the Alma blue staining analysis demonstrated that the antibacterial activity of Au50 nanoparticles is weaker extracellularly (Figure S3C) than intracellularly (Figure S3D), which may aid macrophages in enhancing bacterial clearance. In the meantime, we obtained the same results as in Figure S3D by observing the survival of bacteria cells with live & dead bacterial staining (Figure S3E).



(caption on next page)

Fig. 2. The inflammatory response induced by LPS in macrophages were attenuated by Au50 through the inhibition of MAPK signaling pathway. (A) ELISA analysis of the inflammatory factor secretion of RAW264.7 cells primed with LPS (100 ng/mL, 6 h) and Au nanoparticles (200 μ g/mL, 48 h). (B) RT-PCR analysis of the inflammatory factor secretion of RAW264.7 cells primed with LPS (100 ng/mL, 6 h), Au50 nanoparticles (200 μ g/mL, 48 h), and stimulated with Au50 nanoparticles after LPS treatment. (C) The 10 top category terms of GO enrichment analysis. The y-axes correspond to the GO terms, and the x-axes show the enrichment factor. (D) GSEA enrichment plots showing the two significantly enriched and downregulated signaling pathways, including the inflammatory response of HALLMARK and the MAPK signaling pathway of KEGG. (E) Hierarchical cluster analysis of the 50 top significant differential expression genes in the three downregulated signaling pathways of GSEA enrichment plots in (D). (F) LPS (100 ng/mL, 6 h) and Au50 nanoparticles (200 μ g/mL, 48 h) stimulate RAW264.7 cells respectively or in pairs. The expression levels of related proteins in the MAPK signaling pathway (JNK, ERK, p38, p-JNK, p-ERK and p-p38) were analyzed by western blot.

Previous studies demonstrated that *S. aureus*-infected phagocytes are engulfed by phagocytosis and degraded by lysosome fusion [37–39]. However, *S. aureus* could conceal itself in phagosomes and inhibit autophagy to evade degradation and speed up intracellular proliferation, thereby infecting and invading the cell or organism continuously [28, 40]. We utilized the SYTO41 nucleic acid probe to label *S. aureus* and the LysoTracker to label lysosomes, and observed the intracellular degradation of *S. aureus* using a confocal microscope. The results demonstrate that Au50 nanoparticles can stimulate the formation of lysosomes in RAW264.7 cells (Fig. 4B) and the phagocytosis of macrophages towards *S. aureus*, which was also observed in BMDMs (Figure S3F). Using TEM, the Au50 nanoparticles were primarily distributed in the phagolysosome or the cytoplasm compartments and that *S. aureus* was primarily distributed in the phagosome or the phagolysosome in RAW264.7 cells (Fig. 4C) and BMDMs (Figure S3G).

Analysis of the experimental results described above shows that the Au50 nanoparticles promoted phagocytosis and intracellular sterilization of *S. aureus* in macrophages; however, the molecular mechanism remains unknown. Based on the results of GO enrichment analysis, we selected 6 GO terms associated with bacterial infection and autophagy from the RNA-seq data and created GO chords (Fig. 4D) and a volcano map (Fig. 4E) of the involved genes based on the LogFC sequence. TREM2 was the gene whose expression differed the most between clusters associated with bacterial infection and autophagy, and its expression increased in the LPS + AuNPs cluster. The phagocytosis of myeloid cells was regulated by TREM2, the triggering receptor expressed on myeloid cells-2, and the adaptor protein DAP12 [41]. There are reports in the scientific literature that TREM2 could promote the clearance of macrophages from bacteria and increase the immune resistance of the host [42–44]. As a result, we utilized western blot to verify whether Au50 nanoparticles could induce the expression of TREM2 and DAP12 in RAW264.7 cells (Figure S4A) and BMDMs (Figure S4B) following LPS pretreatment. We utilized siRNA to inhibit TREM2 expression (Figure S4C) and Au50 nanoparticles to stimulate siRNA-treated RAW264.7 cells. After TREM2 silencing in 7 cells, Au50 nanoparticles were unable to stimulate TREM2 expression (Figure S4D). Using TEM, we observed that the phagocytosis of RAW264.7 cells decreased after TREM2 was knocked down and could not be restored by stimulation with Au50 nanoparticles (Figure S4E). Therefore, we infer that Au50 nanoparticles could enhance the bacterial phagocytosis of macrophages by overexpressing TREM2. Additionally, we confirmed the impact of TREM2 knockdown on the autophagy process. After TREM2 knockdown, autophagosomes were labeled with GFP-LC3 lentivirus transfected RAW264.7 cells, lysosomes were labeled with LysoTracker, and *S. aureus* was labeled with SYTO41. Subsequently, the localization or distribution of autophagosomes, lysosomes, and *S. aureus* was observed under the confocal microscope (Fig. 4F). According to our findings, knocking out TREM2 inhibits the phagocytosis of *S. aureus* by cells, and the stimulation of nanoparticles cannot be enhanced. Meanwhile, we observed that *S. aureus* was encapsulated by autophagosomes, but was hardly co-localized with lysosomes and that knocking down TREM2 had no effect. In addition, the formation of lysosomes and the fusion of autophagosomes with lysosomes were promoted, despite the fact that Au50 nanoparticles did not increase the phagocytosis of macrophages with TREM2 knockdown. Therefore, we hypothesized that TREM2 was the key gene for Au50 nanoparticles to induce macrophages to phagocytose *S. aureus*. However, TREM2 does not interfere with *S. aureus* in autophagosomes to prevent the fusion of lysosomes with it, whereas the intracellular sterilization of

macrophages by Au50 nanoparticles treatment promoted the fusion of autophagosome-lysosome.

2.5. The autophagosome-lysosomal fusion was promoted to clear intracellular *S. aureus* by Au50 inducing VAMP8 to bind STX17 and SNAP29

To validate our hypothesis, we analyzed the RNA-seq data. The GSEA analysis was then used to uncover the underlying mechanisms of intracellular sterilization of macrophages induced by Au50. The results suggested that the two upregulated pathways, Protein localization to lysosome of GOBP and Lysosome of KEGG, were significantly enriched in cluster LPS + AuNPs (Fig. 5A). In RAW264.7 cells, we detected autophagy-related proteins, including autophagy precursor-related proteins BECLIN1, ATG5, ATG12, and ATG16L1, as well as autophagosome protein LC3B, autophagy flow degradation-related protein SQSTM1, and lysosomal marker protein LAMP1 (Fig. 5B). The results demonstrated that the expression of autophagic flux and autophagic degradation increased, while the expression of lysosome marker protein increased but lysosome-autophagosome fusion was inhibited. The expression levels of the aforementioned major proteins follow the same pattern in BMDMs treated with the same agent (Figure S5A). Subsequently, we treated cells with LPS for 6 h before administering Au50 nanoparticles based on various time gradients. The expression of autophagy-related proteins and lysosomal marker proteins increased over time, whereas the expression of autophagy degradation-related proteins decreased (Fig. 5C). BMDMs also yielded the same results (Figure S5B).

mRFP-GFP-LC3 (mRFP: Red Fluorescent Marker; GFP: Green Fluorescent Marker) was utilized to monitor autophagic flux in more detail. During the initial phase of autophagy, mRFP-GFP-LC3 aggregates on autophagosomes, forming red/green co-localized dots. Then, autophagosomes fuse with lysosomes, leading to the formation of autophagic lysosomes. Because the acidic environment of lysosomes leads to the quenching of GFP, only orange fluorescent spots can be detected. Thus, autophagosomes in cells are represented by bright yellow dots (overlapping green and red fluorescence), whereas autophagosomes are represented by orange dots (quenched green fluorescence). Therefore, RAW264.7 cells were transfected with mRFP-GFP-LC3 adenovirus; Then, macrophages were cultured with or without Au50 nanoparticles and treated with *S. aureus* for 6 h; Finally, Gentamycin was used to kill the extracellular bacteria and SYTO41 probe was used to label the intracellular *S. aureus*. Subsequently, fluorescent spots were detected using a confocal microscope (Fig. 5D). The results showed that the number of orange spots significantly increased after Au50 treatment, indicating that the autophagic flux in macrophages was activated. After incubation with *S. aureus*, the number of bright yellow spots increased significantly and co located with blue spots, while the number of red spots decreased, indicating that *S. aureus* hid in autophagosomes to inhibit the formation of autophagic lysosomes. In contrast, compared with not treated with Au50, the number of orange spots in macrophages treated with Au50 was significantly increased when incubated with *S. aureus*, indicating that Au50 nanoparticles could restore the autophagic flux blocked by *S. aureus*. Similarly, we observed an identical phenomenon in BMDMs receiving the same treatment (Fig. S5C).

In addition, we investigated the molecular mechanism by which Au50 nanoparticles promote autophagic flow. Previous studies have confirmed that STX17 was recruited as a transmembrane SNARE protein on

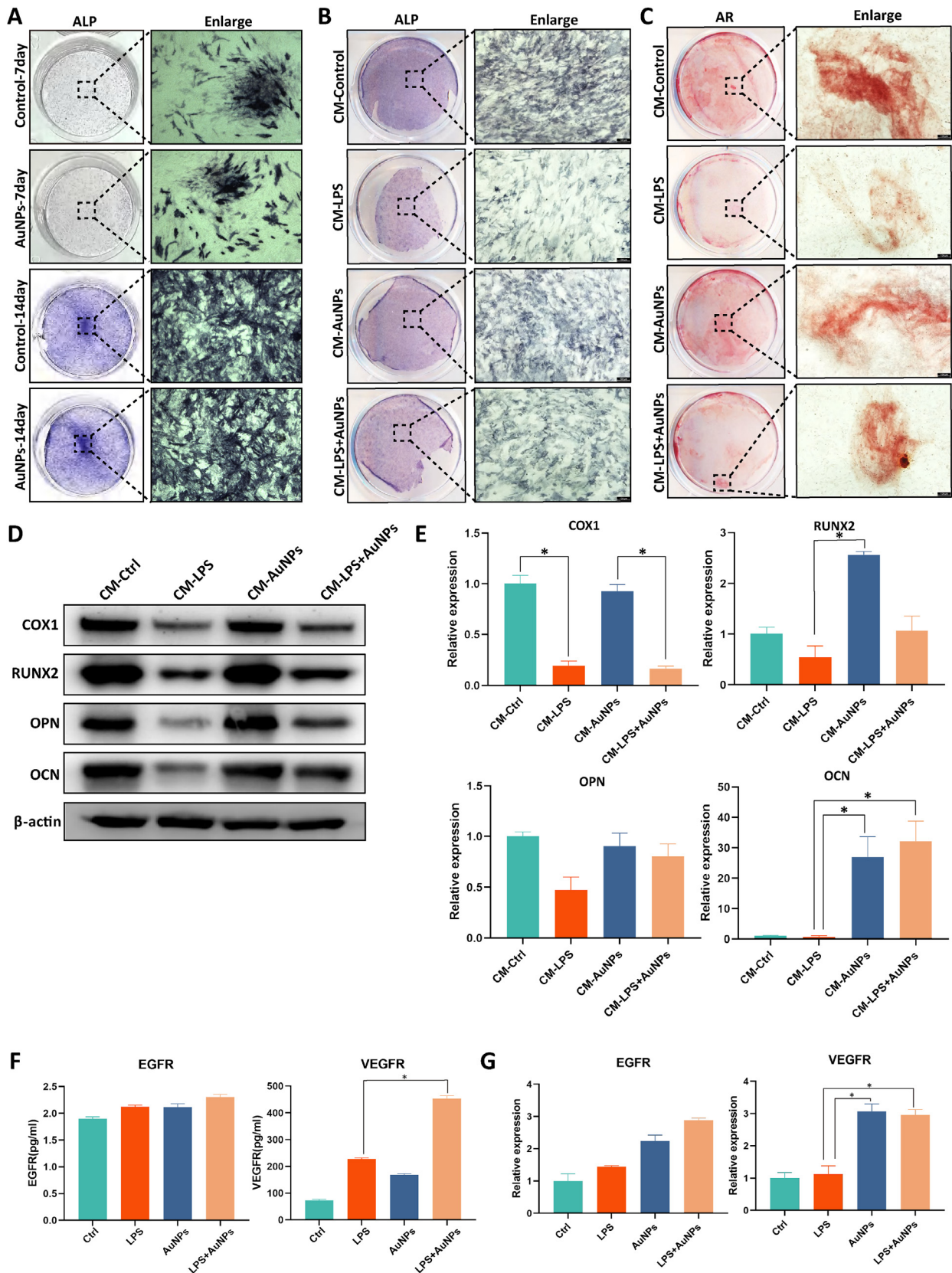
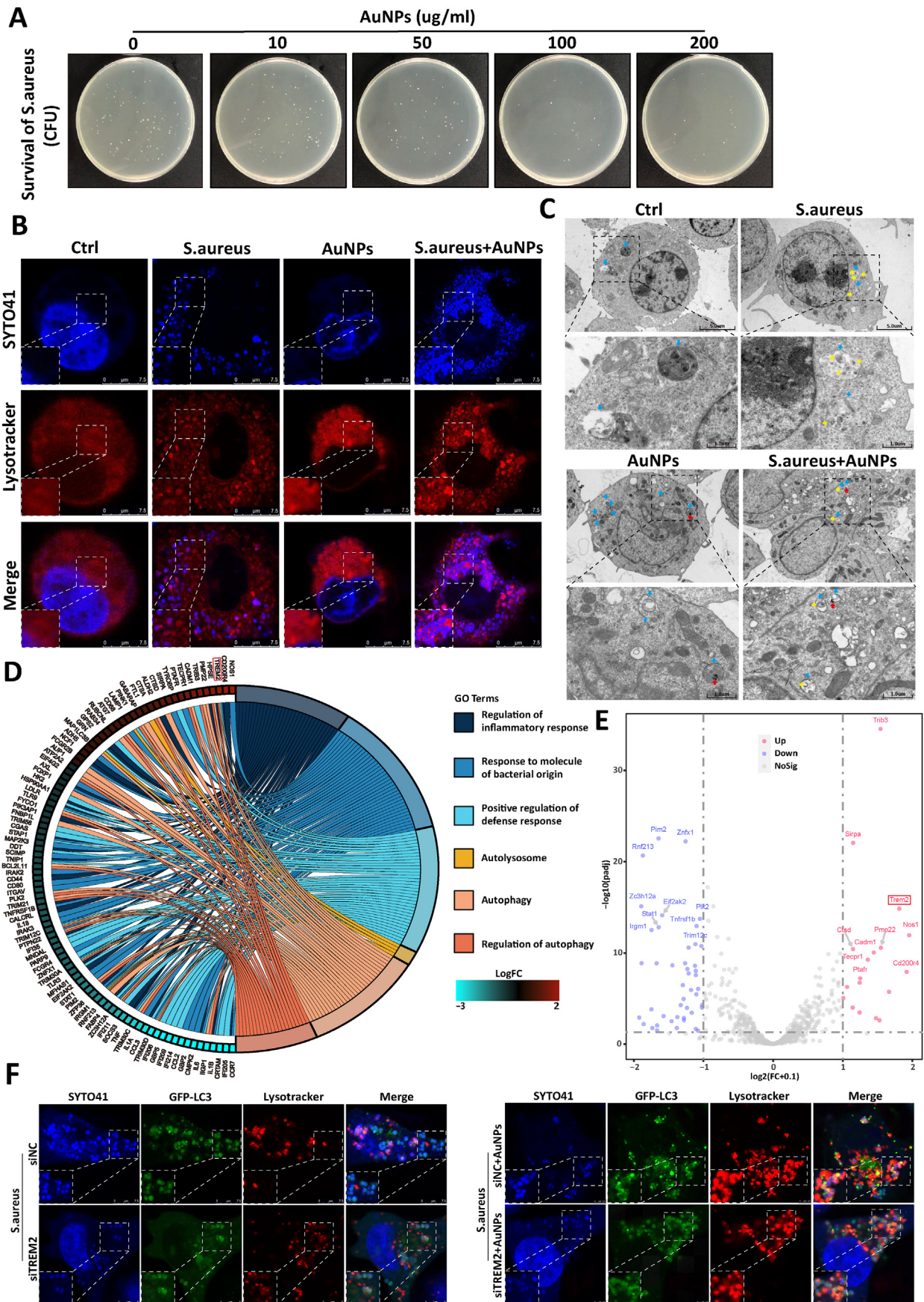


Fig. 3. The osteogenesis and vascular differentiation of peripheral cells were promoted by Au50 reducing the secretion of inflammatory factors in macrophages. (A) The osteogenic differentiation was analyzed by ALP staining. Conditional medium with different treatments stimulates BMSCs for the detection of osteogenic differentiation; the osteogenic differentiation was analyzed by ALP staining (B) and AR staining (C), the related proteins, Cox1, Runx2, Opn, and Ocn protein levels were analyzed by western blot (D) and RT-PCR (E). The detection of angiogenic differentiation with different treatments stimulates RAW264.7 cells for the secretion of related cytokines, EGFR and VEGFR were analyzed by ELISA (F) and RT-PCR (G).



(caption on next page)

Fig. 4. The phagocytosis and intracellular sterilization of macrophages to *S. aureus* was promoted by Au50 induce overexpressing TREM2. (A) Representative LB plate image of CFUs of *S. aureus* for the bactericidal assay in LB culture medium. (B) The phenomenon of *S. aureus* being phagocytosed by RAW264.7 cells was visualized and imaged using a confocal microscope. The red fluorescence showed that lysotracker was in the cytoplasm after treatment. The blue fluorescence showed that the nuclear and *S. aureus* stained by SYTO41. (C) The intracellular location of Au50 nanoparticles and *S. aureus* were analyzed by TEM in RAW264.7 cells after treatment. The red arrows indicate Au50 nanoparticles, the yellow arrows indicate *S. aureus* and the blue arrows indicate the autolysosome. (D) The chordal and (E) the volcano plots of GO enrichment analysis of autophagy and bacterial resistance in RAW264.7 cells after treatment. (F) The phenomenon of *S. aureus* being phagocytosed and cleared from the intracellular environment by RAW264.7 cells, with or without Au50 nanoparticles treatment after transfection with TREM2 siRNAs was visualized and imaged using a confocal microscope. The green fluorescence showed that autophagosome and red fluorescence showed that lysotracker was in the cytoplasm after treatment. The blue fluorescence showed that the nuclear and *S. aureus* stained by SYTO41. (For interpretation of the references to colour in this figure legend, the reader is referred to the Web version of this article.)

autophagy at the onset of autophagy, forming a ternary SNARE complex with SNAP29 and VAMP8 to mediate autophagy-lysosome fusion. Correspondingly, the autophagy-lysosome was formed and STX17 was transferred to the lysosome after lysosome formation [45]. Consequently, the interaction between STX17 and two SNARE proteins was essential for autophagosome and lysosome fusion [46,47]. Therefore, the RAW264.7 cells were stimulated according to the previous protocol, and Co-IPs were performed to determine whether the proteins formed complexes. These results demonstrated that the binding of VAMP8 with STX17 and SNAP29 was increased in Au50 nanoparticles, which may be related to the increased expression of VAMP8 protein induced by Au50 nanoparticles. However, the binding of STX17 with SNAP29 did not demonstrate a significant difference (Fig. 5E, Figure S5D, Figure S5E). These experiments demonstrated that Au50 nanoparticles promoted autophagic flux to eliminate intracellular *S. aureus* by enhancing the combination of VAMP8 with STX17 and SNAP29, which is achieved by elevating VAMP8 expression.

2.6. The regeneration of infectious tissue defect in rat was accelerated by Au50

Encouraged by the excellent biocompatibility, anti-inflammatory activity, and effective intracellular and extracellular antibacterial activity of the prepared AuNPs, Au50 nanoparticles were selected and used to evaluate the in vivo wound healing performance in a rat model with infectious tissue defect. We selected the most commonly used osteomyelitis and full-thickness skin defect models in the tissue infectious defect model. The in vivo therapeutic potential of the AuNPs was finally evaluated in a bacteria-infected bone defect (osteomyelitis) model. Following the creation of a 0.3 cm circular defect in the femur of a rat, 10^8 colony-forming units (CFU) of *S. aureus*, a major bacterial strain used in clinics to induce osteomyelitis, were injected to induce bone infection [48]. Subsequently, the bone defects of each group were filled with a sterile gel sponge, the weight of rats in each group was recorded weekly (Figure S6B), and the overall appearance was observed 42 days after treatment (Figure S6A) to calculate the healing area of bone defects (Fig. 6B). On the 42nd day, bone defect area of the defective control group (Bone Defect Healing Rate, BDHR: $94.08\% \pm 1.29\%$) and the *S. aureus* group that had been treated with Au50 nanoparticles (BDHR: $89.67\% \pm 3.66\%$) demonstrated the smallest area compared to the native *S. aureus* group (BDHR: $26.11\% \pm 8.59\%$). After treatment with sterile blank gel, X-ray (Fig. 6A) and Micro-CT (Fig. 6C) reveal progressive cortical bone destruction in the femur of the bacterial infection group, whereas the bone defect in the Au50 nanoparticles treatment group has recovered with minimal holes remaining. In the study of micro-CT analysis of cortical bone and trabecular bone in rats with bone infection, we observed significant results between *S. aureus* and Au50 groups, in which BV/TV, BMD, Tb-Th and Tb-N values were lower but Tb-SP values were higher, which may be because long-term bacterial infection may cause serious damage to the trabecular bone microstructure of these two groups (Fig. 6D & S6C). Compared with the untreated group, we observed the increase of BMD, BV/TV, Tb-N value and the decrease of Tb-SP value in the infected rats treated with Au50 (Figure S6C), equivalent to defect control group, indicating that Au50 nanoparticles ameliorated the properties of trabecular bone in infected rats. Although

bone tissue in the Au50 treatment group regenerates gradually and long-term Au50 treatment significantly reduces the number of living bacteria in the bone marrow, after 42 days there is no visible bacterial colony (Figure S6D).

Histological analysis with HE staining, Masson trichrome, Safranin O and Gram staining was then conducted to further clarify the quality of regenerated bone defect tissue infected by *S. aureus* among the three groups. HE staining of the femoral medullary cavity of each group is presented in Fig. 6E. In *S. aureus* group, intramedullary abscess formation and massive inflammatory cell infiltration were observed. In contrast, the infection in the Au50 nanoparticle treatment group was basically controlled, and only slight inflammatory reaction remained, which may be related to the stimulation of *S. aureus* degradation products on surrounding tissues. In order to further evaluate the effect of Au50 nanoparticles, Masson staining was performed on the femoral medullary cavity (Fig. 7A). More immature sequestrum formation in *S. aureus* group, however, it has better bone mass after treatment with Au50 nanoparticles. Safranin O staining of sections (Figure S6E) showed that the new bone trabeculae in the defect control group and the Au50 group contain typical porous structures with a large number of osteoblasts around them. Such porous structure is conducive to related communication and aggregation of bone factors, as well as the migration, proliferation, and differentiation of BMSCs, which is conducive to bone defect repair. Compared with *S. aureus* group, Au50 group has more new bone and more orderly trabecular structure, which indicates that adding Au50 nanoparticles can significantly promote the formation of new bone and repair of bone defects. In addition, compared with the residual infection in the *S. aureus* group, Gram staining showed that the bacterial infection in the group treated with Au50 nanoparticles has been cured (Figure S6F).

In order to further verify the mechanism of Au50 promoting the bacteriostasis of phagocyte in tissues, we detected the co localization of TREM2 (red point), LC3B (green point) and LAMP1 (yellow point) in different groups by immunofluorescence. The results showed that the expression of TREM2 and LAMP1 was significantly reduced in the infection group, and the co-localization of LC3B and LAMP1 was significantly reduced. However, the expression of TREM2 and LAMP1, as well as the co-localization of LC3B and LAMP1, were significantly increased in the Au50 treatment group (Figure S7A). Subsequently, we tested the immunofluorescence co-localization of STX17 (yellow point), VAMP8 (green point) and SNAP29 (red point) in tissues and found that VAMP8 expression decreased and co-localization with STX17 and SNAP29 decreased in the infection group, while recovery was observed after Au50 treatment (Figure S8A). In addition, we also detected the polarization of macrophages in tissues through immunofluorescence, and found that the expression of CD86 (red point) was significantly increased in the infection group, while the expression of CD206 (green point) was significantly enhanced in the Au50 treatment group (Figure S9A). Therefore, we also validated the mechanism of Au50 promoting macrophage clearance of bacteria in vitro experiments.

Immunohistochemical staining was performed on all three treatment groups in order to elucidate the anti-inflammatory properties of the Au50 nanoparticles. As an in vivo proinflammatory cytokine, TNF- α is the primary mediator of the inflammatory response of the host. CD31, also known as platelet endothelial cell adhesion molecule, is primarily

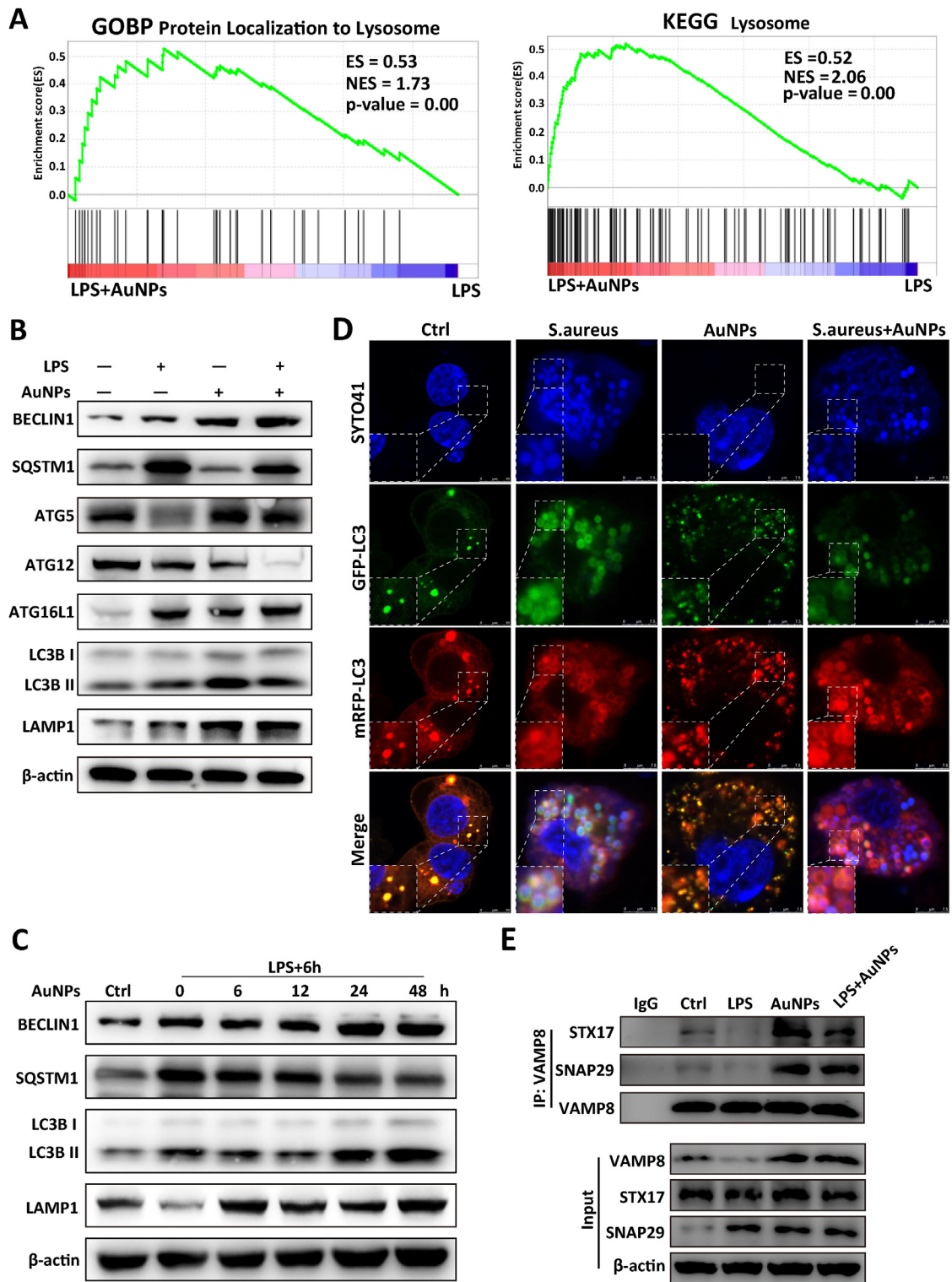


Fig. 5. The autophagosome-lysosomal fusion was promoted to clear intracellular *S. aureus* by Au50 inducing VAMP8 to bind STX17 and SNAP29. (A) GSEA enrichment plots showing the two significantly enriched upregulated signaling pathways including the protein localization to lysosome of GOBP and the lysosome of KEGG. (B) LPS and Au50 nanoparticles stimulate RAW264.7 cells respectively or in pairs. Related proteins in autophagy, Beclin1, Sqstm1, Atg5, Atg12, Atg16L1, Lc3b, and Lamp1 protein levels were analyzed by western blot. (C) LPS was used to stimulate RAW264.7 cells, and then stimulated with Au50 nanoparticles at different time intervals. Related proteins in the autophagy, Beclin1, Sqstm1, Lc3b and Lamp1 protein levels were analyzed by western blot. (D) The phenomenon of autophagosome-lysosomal fusion to clear the intracellular *S. aureus* by RAW264.7 cells after infection with mRFP-GFP-LC3 lentivirus with or without Au50 nanoparticles treatment was visualized and imaged using a confocal microscope. The green and red fluorescence showed that autophagosome was in the cytoplasm after treatment. The blue fluorescence showed that the nuclear and *S. aureus* stained by SYTO41. (E) LPS and Au50 nanoparticles stimulate RAW264.7 cells respectively or in pairs, and subjected to immunoprecipitation using IgG and anti-VAMP8 antibody. Input and pellet fractions were analyzed by western blot using the antibodies indicated. (For interpretation of the references to colour in this figure legend, the reader is referred to the Web version of this article.)

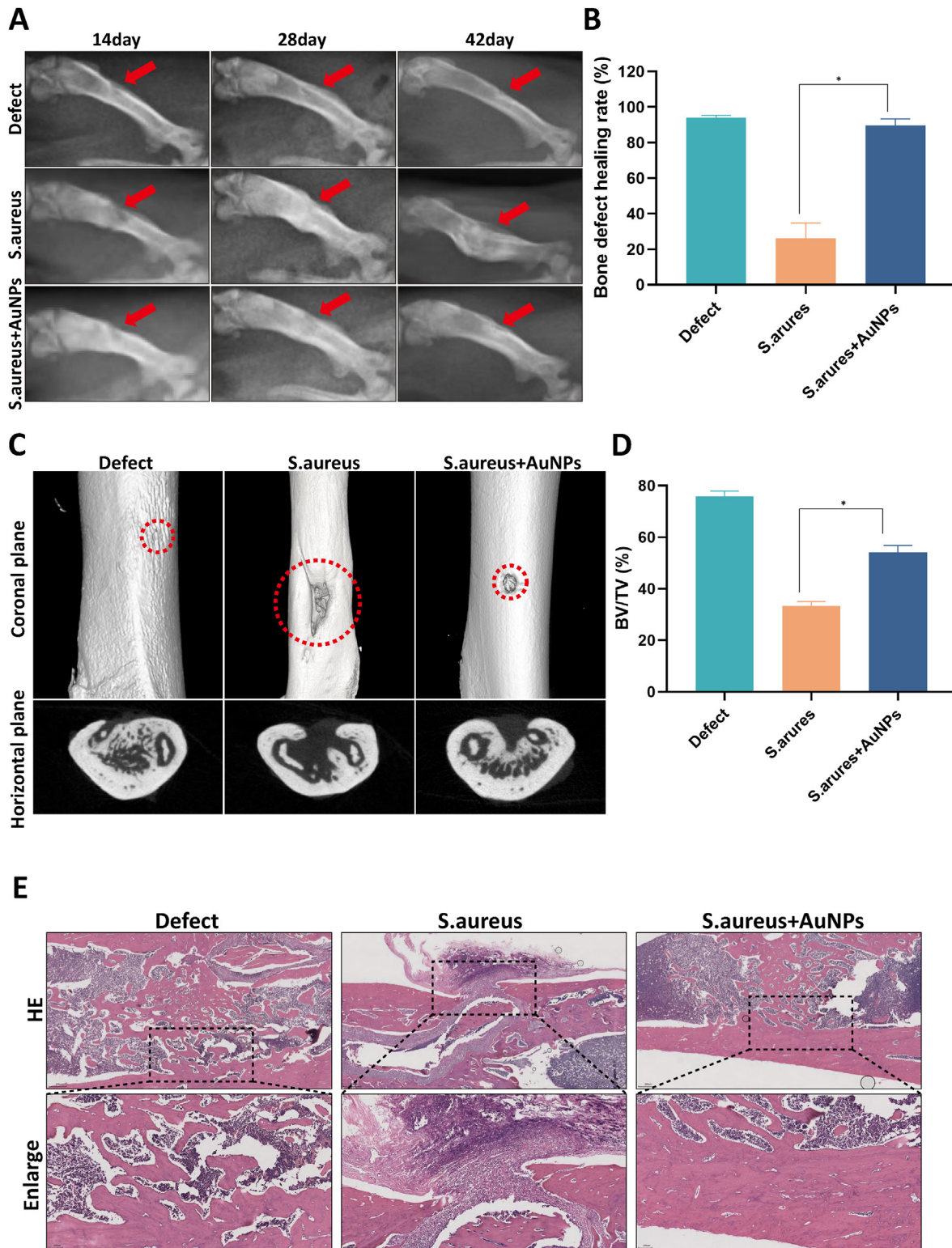


Fig. 6. The repair of femoral osteomyelitis in rats was accelerated by Au50. (A) X-ray image of femoral osteomyelitis in rats at 14 days, 28 days, and 42 days after treatment in each group and the bone defect healing rate (B). The red arrow indicates the bone defect of osteomyelitis. (C) The micro-structure of the femoral infectious defect was analyzed by micro-CT, including coronal plane and horizontal plane and the BV/TV were measured (D). (E) H & E staining of femoral osteomyelitis of rats in each group after 42 days of treatment. (For interpretation of the references to colour in this figure legend, the reader is referred to the Web version of this article.)

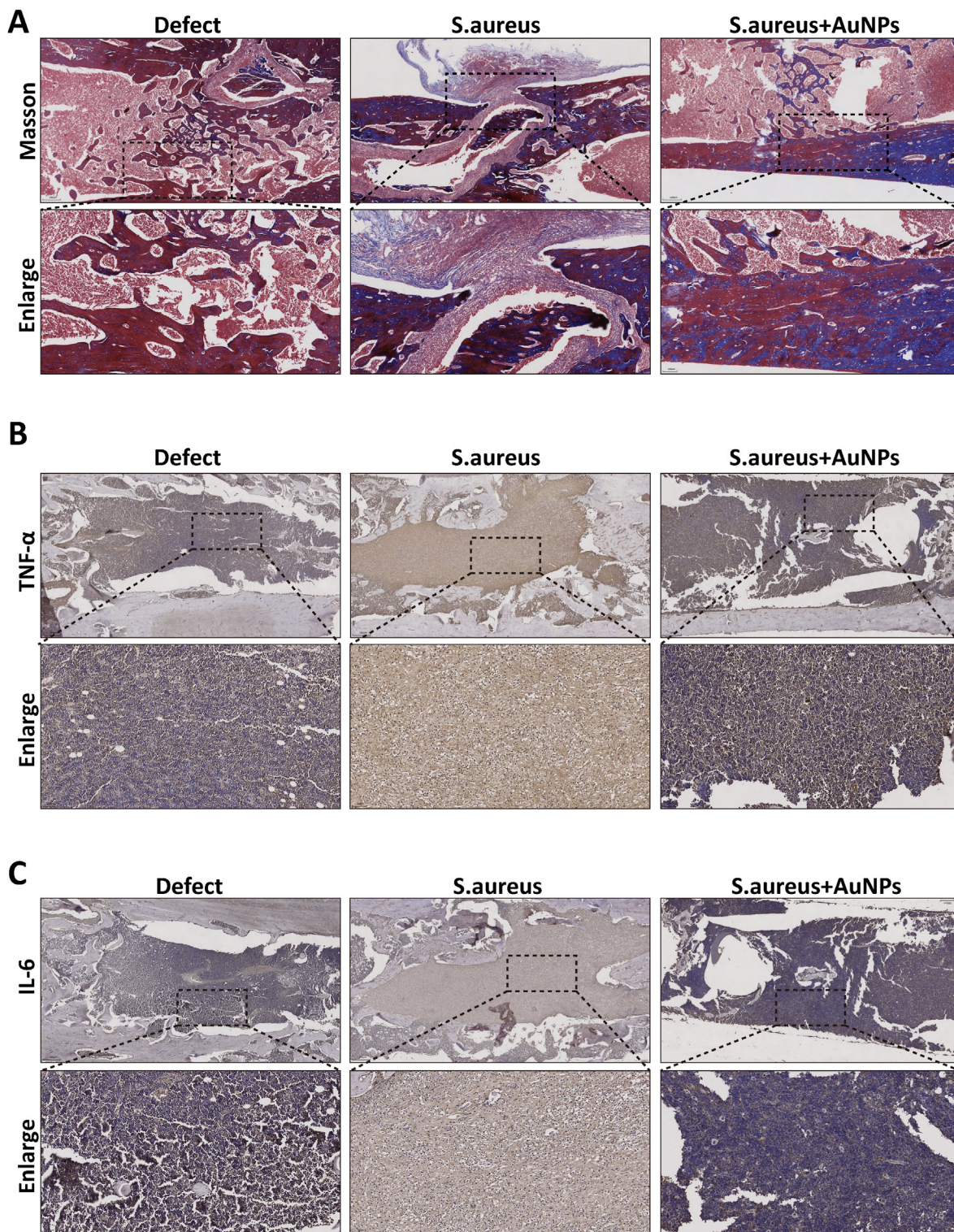


Fig. 7. The Au50 inhibit the secretion of inflammatory factors in vivo. (A) Masson staining of femoral osteomyelitis of rats in each group. Representative immunohistochemical TNF- α (B) and IL-6 (C) stained wound sections in each group.

utilized to demonstrate the presence of endothelial cells and to assess angiogenesis. By inhibiting the release of growth hormones, an increase in TNF- α has the potential to delay wound healing [49]. We have verified the anti-inflammatory effect of Au50 nanoparticles in vivo in the model of infectious skin defect, and we have also found the same effect in the model of osteomyelitis. Immunohistochemical staining of all three

treatment groups showed that the infected *S. aureus* group treated with Au50 nanoparticles showed lower TNF- α (Fig. 7B) and IL-6 (Fig. 7C) secretion or higher CD31 (Figure S9B) and TGF- β (Figure S9C) secretion than the infected *S. aureus* group, and the difference was statistically significant ($p < 0.05$) (Figure S9D-G). These results indicate that Au50 nanoparticles can inhibit inflammation and promote tissue repair in

infected tissues. In addition, for nanoparticles used in vivo, we examined the toxicity of the major organs of rats and determined that Au50 would not be toxic in vivo (Figure S9H).

Finally, the in vivo performance of Au50 nanoparticles in the treatment of infected wounds was investigated (Figure S10A, Figure S10B). On the 3rd, 7th, and 14th day, wound contraction in the *S. aureus* group treated with Au50 nanoparticles (*S. aureus* + AuNPs Group) was superior to other *S. aureus* group (*S. aureus* Group) and comparable to the defective control group (Defect Group). On the 3rd day, wounds of the defective control group (Wound Healing Rate, WHR: $52.08\% \pm 4.17\%$) and the *S. aureus* group that had been treated with Au50 nanoparticles (WHR: $39.68\% \pm 2.09\%$) demonstrated the smallest area compared to the native *S. aureus* group (WHR: $27.03\% \pm 3.67\%$). Importantly, at the 7th day, the *S. aureus* group treated with AuNPs (WHR: $72.33\% \pm 3.68\%$) had a higher wound healing rate than the native *S. aureus* group (WHR: $52.98\% \pm 4.43\%$), whereas the defective control group (WHR: $79.88\% \pm 3.23\%$) and the *S. aureus* group treated with AuNPs remained at the same level, indicating that wounds of the *S. aureus* group treated with AuNPs healed faster than that of the native *S. aureus*. On the 14th day, wounds for *S. aureus* treated with AuNPs (WHR: $98.92\% \pm 0.52\%$) and defective control group (WHR: $99.93\% \pm 0.83\%$) were observed to have healed, whereas wounds for *S. aureus* group (WHR: $88.70\% \pm 2.95\%$) did not appear to have healed. Meanwhile, we also recorded the weight of rats in each group on days 3, 7, and 14.

As shown in Figure S10C, all groups regenerated new epidermis at the wound site 14 days after treatment. Compared with the other two groups, *S. aureus* dressings showed different degrees of inflammatory cell infiltration around the wound, suggesting that AuNPs are beneficial to reduce inflammatory response and promote epidermal remodeling. Furthermore, at day 14, hair follicle and angiogenesis were observed in *S. aureus* treated with Au50 nanoparticles. No significant skin appendage regeneration was observed in the *S. aureus* group, which still contained a large amount of immature tissue. Collagen fibers are a key component of granulation tissue and the extracellular matrix of the dermis. Furthermore, they play a crucial role in wound healing in cell differentiation, tissue repair, and organ nutrition [50]. The amount of collagen deposited at the wound site is also an important indicator of the success of wound repair [51]. Therefore, we used Masson's trichrome staining and blue-stained collagen to determine total collagen levels in the healing wounds to further assess wound healing progress with each of the three treatments. After 14 days of healing, as shown in Figure S10D, the *S. aureus* group treated with Au50 nanoparticles developed relatively denser and more continuous mature collagenous fibers than the defective control group. This suggests that, macroscopically, the *S. aureus* group treated with Au50 nanoparticles was comparable to the defective control group for wound contraction (Figure S10A), and superior to the *S. aureus* group due to a higher collagen level. In addition, Gram staining revealed that the bacterial infection in the *S. aureus* group treated with Au50 nanoparticles was essentially cured, whereas the *S. aureus* group was still infected 14 days after healing (Figure S11B).

In order to evaluate the level of inflammation in wound tissue on days 3, 7, and 14, TNF- α and CD31 expression were measured. As shown in Figures S11C, the infected *S. aureus* group treated with Au50 nanoparticles exhibited lower TNF- α expression than the infected *S. aureus* group at each detection timepoint. On the third day, there was a statistically significant difference between the infected *S. aureus* group that was treated with Au50 and the infected *S. aureus* group that was not treated (Figure S11C). As shown in Figure S11D, the *S. aureus* group had the lowest level of CD31 expression overall, with statistical difference compared with the other two groups. These results also confirm our previous findings that compared with the *Staphylococcus aureus* group, the Au50 treatment group has a significant effect on the inhibition of TNF- α level, the inhibition of inflammatory reaction and the stimulation of angiogenesis are better. Similarly, we examined the toxicity of the major organs of rats and determined that Au50 would not be toxic in vivo (Figure S11E).

3. Discussion

Although systemic administration of antibiotics typically results in the cure of the majority of infectious diseases, more effective dose is required in the case of infectious tissue defect such as osteomyelitis or skin defect due to its unique anatomical characteristics, which result in the treatment concentration of antibiotics being continuously below the MIC for invasive pathogens [52]. Widespread use of PMMA beads containing antibiotics has significantly improved osteomyelitis treatment outcomes in clinical practice. However, poor release kinetics leads to insufficient drug elution, and the thermal energy of polymerization may result in host tissue damage [53]. The surface ratio and the number of atoms near the surface of nanomaterials vary with particle size, which explains why the properties of nanomaterials with different particle sizes are obviously distinct. Therefore, based on the numerous advantages of nanomaterials, such as their large surface area-to-mass ratio, good mechanical properties, and biocompatibility, they can be used to involve highly specific materials and interact with human cells at the molecular level to achieve the greatest therapeutic effect with the fewest side effects [54,55]. In recent years, an increasing number of researchers have examined the differences between the effects of nanomaterials with different particle sizes, shapes, and structures on cells, and then the role of nanomaterials themselves [56–59]. This study, therefore, investigated the various functions of gold nanoparticles with varying particle sizes and the underlying molecular mechanism and developed Au50 nanoparticles as a promising nanomaterial for the treatment of infection in vivo.

Previous research has demonstrated that stem cells play a role in tissue repair, and the osteoblastic differentiation of stem cells is affected differently by various nanoparticle shapes and sizes [60–63]. As confirmed from our findings, Au50 nanoparticles can induce RAW264.7 cells and BMDMs M2 polarization to weaken inflammatory response through the inhibition of NF- κ B and MAPK signaling pathways, as well as promote BMSC osteogenic differentiation in a conditioned medium environment. We did not observe the macrophage polarization response when NF- κ B or MAPK activator was used, nor did we observe the decrease in LPS-induced macrophage M1 polarization when NF- κ B or MAPK inhibitor was used. However, we observed the decrease in M1 polarization when NF- κ B and MAPK activator was used, and partial induction of M2 polarization when NF- κ B and MAPK inhibitor was used in macrophages. Accordingly, we hypothesized that the polarization of macrophage M1 was related to many factors, of which the NF- κ B and MAPK pathways were only a part. However, when LPS-triggered M1 polarization occurred, inhibiting NF- κ B and MAPK could restricted M1 polarization and partially transform into M2 polarization. We believe that the M2 polarization effect induced by Au50 in macrophages is not entirely regulated by the NF- κ B and MAPK signaling pathways, but is partially regulated or caused by the interaction of multiple pathways, which requires further investigation.

Previous research has demonstrated that the antibacterial capability of gold nanoparticles is dependent on their morphology, with star- and flower-shaped nanoparticles exhibiting the most potent antibacterial effects [64]. In addition, the antibacterial mechanisms of AuNPs against various bacteria vary. AuNPs eliminate bacteria in *S. aureus* by increasing ROS production and inhibiting DNA transcription [65,66]. AuNPs can induce vesicle formation and combine with DNA to inhibit transcription in *Escherichia coli* in order to resist bacterial infection [66,67]. In *Streptococcus pneumoniae*, AuNPs form inclusion bodies within bacteria to destroy biofilm and serve an antibacterial function [68]. AuNPs can also cause intracellular bivalent cation homeostasis to break down. Antibiotics can induce the accumulation of intracellular ROS. The synergistic effect of the two can result in the death of salmonella cells via apoptosis [69]. In the phagocytic phase, we discovered that the overexpression of TREM2 in macrophage induced by Au50 nanoparticles enhanced macrophage bacterial phagocytosis. TREM2 is a macrophage phagocytic receptor that controls macrophage immune function by fine-tuning ROS production and boosts the host's defense against bacterial infection [43,

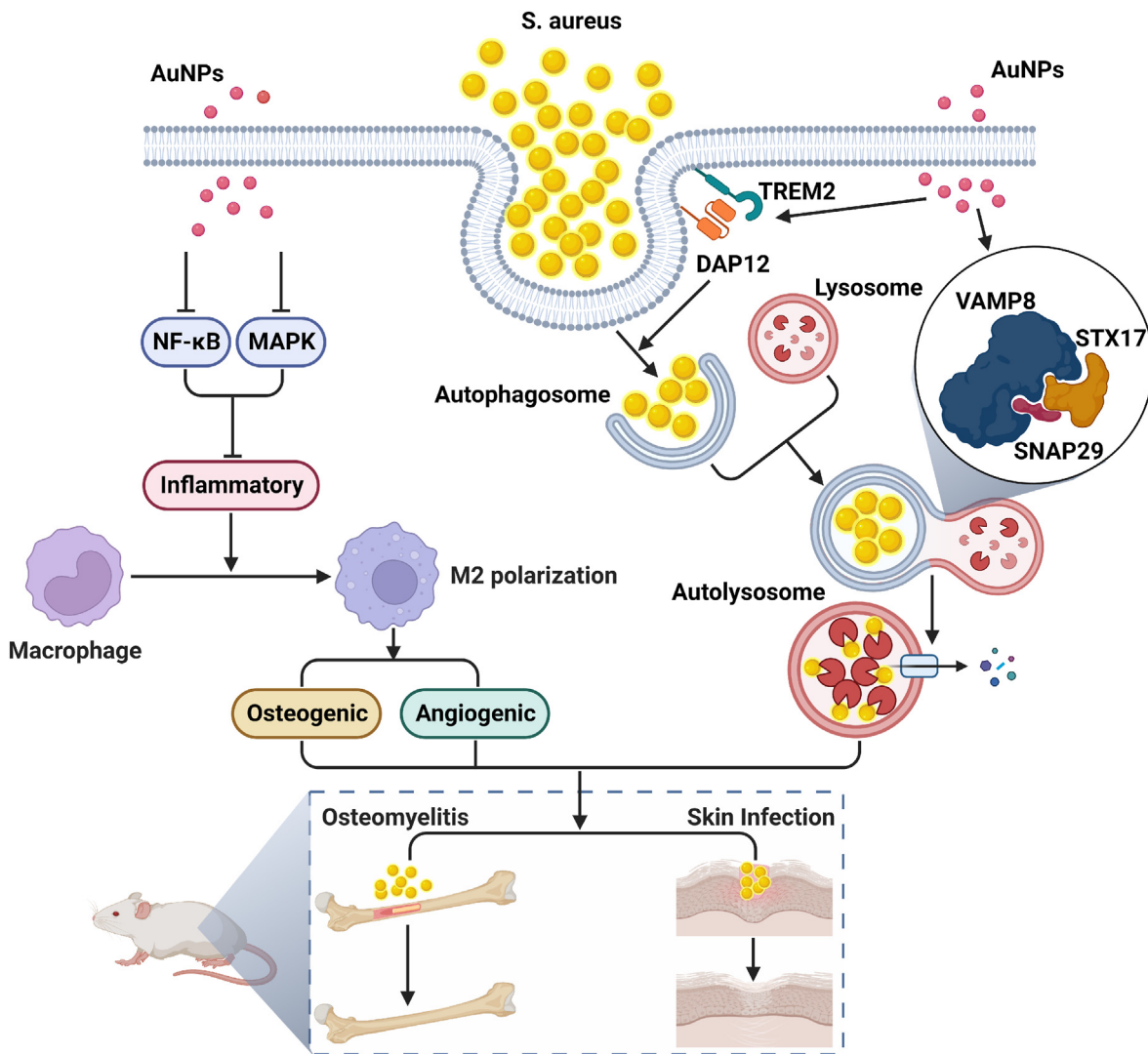


Fig. 8. Scheme illustration for Au50 promoting tissue repair of *S. aureus* infection. Au50-nanoparticle-induced infective tissue repair requires dual function: (1) Au50 nanoparticles promote macrophages M2 polarization and reduce the secretion of inflammatory factors through the inhibition of NF- κ B and MAPK signaling pathways to promote tissue regeneration and (2) improving phagocytosis of macrophages by overexpressing TREM2 and enhance the interaction of VAMP8 with STX17 and SNAP29 to promote the fusion of autophagosomes and lysosomes to eliminate intracellular bacteria. Through dual functions, Au50 nanoparticles promotes the regeneration of infected skin defects and the repair of femoral osteomyelitis in rats. Created with BioRender.com.

70]. We discovered that phagocytosis of macrophages decreased significantly following the knockdown of TREM2 with siRNA, whereas Au50 could not increase the gene expression level of TREM2 following the knockdown of siRNA. This may be associated with the site at which Au50 stimulates TREM2 expression, which requires further investigation. In the context of intracellular bacterial elimination, our research demonstrates that Au50 nanoparticles degrade *S. aureus* hiding in autophagosomes by promoting autophagosome-lysosome fusion. During autophagy, autophagosomes ingest pathogens, organelles, and bacteria before transporting them to lysosomes for degradation. The fusion of autophagosomes and lysosomes is essential for the autophagic flow to proceed smoothly [71]. STX17 was recruited to autophagosomes during the process of fusion. STX17 formed a SNAP ternary complex with SNAP29 on the autophagosome membrane and VAMP8 on the lysosome membrane to mediate the fusion of autophagosome and lysosome after autophagosome phagocytosis bacteria reached maturity. After autophagy lysosome formation, STX17 translocated to the lysosome and then exited the lysosome [45,72]. Therefore, we found that Au50 nanoparticles promote the formation of SNAP ternary complex by promoting the

combination of VAMP8 with STX17 and SNAP29, which may be related to inducing the overexpression of VAMP8. We believe that this is the key to its ability to promote the fusion of autophagic lysosomes and thus enhance the autophagic process of intracellular bacteria. To determine whether Au50 affects the lysosomal translocation of STX17, more research is required to determine the precise binding site and mode of Au50, which stimulates the binding of SNAP ternary complex.

To summarize, we demonstrated in vitro that Au50 nanoparticles can induce M2 polarization of macrophages to diminish inflammatory response, as well as induce intracellular bacterial degradation by promoting the fusion of autophagosomes and lysosomes. Meanwhile, we constructed in vivo rat models of infectious skin lesions and osteomyelitis to confirm that Au50 has clinical potential for accelerating the repair of infectious tissue damage (Fig. 8).

4. Conclusions

In conclusion, our study demonstrates that the diameter of nanoparticles plays a crucial role in determining the polarization effect on

macrophages. The size of 50 nm gold nanoparticles is optimal for promoting macrophages M2 polarization and inhibiting the secretion of inflammatory factors. In addition, we confirmed that Au50 can enhance the phagocytosis of macrophages toward *S. aureus* by overexpressing TREM2 and promoting the interaction of VAMP8 with STX17 and SNAP29 to enhance the fusion of autophagosome lysosomes and induce the degradation of intracellular bacteria. In addition, Au50 nanoparticles with their good biocompatibility have been demonstrated to be effective biomaterials for the treatment of infection in vivo, while Au50 nanoparticles can also down-regulate inflammatory response-related pathways, reduce the secretion of inflammatory factors, and promote bone formation and vascular differentiation by promoting macrophage secretion of repair promoting factors, so as to speed up the tissue regeneration of infected sites. Due to their properties of promoting macrophage phagocytosis, sterilization, and repair, Au50 nanoparticles have a high clinical potential in the treatment of infection in vivo.

5. Materials and methods

5.1. Synthesis of Au nanoparticles

All necessary glasswares were soaked in aqua regia for 24 h, and then used after drying. Subsequently, sodium citrate was added to 150 mL of ultrapure water, heated to 110 °C, followed by the addition of HAuCl₄ to react for 10 min. The resultant solution was then cooled to 90 °C, and sodium citrate and HAuCl₄ were added over the course of 2 min, to allow a subsequent reaction of 30 min. The preceding steps were then repeated to obtain gold nanoparticles with varying particle sizes.

5.2. Dynamic light scattering analysis

The hydrodynamic diameter and zeta potential of AuNPs were determined by dynamic light scattering (DLS) in a submicron particle size and zeta potential analyzer manufactured by Beckman Coulter called DelsaNano C. Number distribution on a normalized scale was used to conduct measurements. At 25 °C DEME was used as a dispersing medium for the measurements (viscosity 0.8872 cP; dispersant dielectric constant 78.5; dispersant refraction index 1.330). To conduct DLS analysis, both AuNPs and AuNPs (2 mg/mL) stocks were diluted 1:1 v/v.

5.3. Macrophage cell culture

RAW264.7 cells were obtained from the American Type Culture Collection (ATCC) and cultivated in RPMI 1640 medium (Gibco) supplemented with 10% heat-inactivated foetal bovine serum (Gibco) at 37 °C and 5% CO₂. C57 mice aged 4–6 weeks were anesthetized and then decapitated. The femur and tibia were uncovered by slicing the skin. Subsequently, the bone fragments from above the hip joint and below the knee joint were placed in the sterile culture medium. A 10 cm culture dish was then taken, and the severed ends of the femur or tibia were placed therein, to flush the bone marrow into the culture dish using a 1 mL syringe. Subsequently, macrophages derived from bone marrow were cultured in DMEM medium (Gibco) supplemented with 10% heat-inactivated foetal bovine serum (Gibco) and 30 ng/mL *M-CSF* (Pepro- tech, USA) at 37 °C and 5% CO₂.

5.4. Transmission electron microscopy analysis

The physical characterization of synthesized AuNPs was accomplished by TEM using JEM-1230 (JEOL company, Peabody, MA) instrument working at an accelerating voltage of 100 kV. More than 100 particles were measured in a random field of vision, and the average particle size and standard deviation were calculated using images. The collected data were analyzed by ImageJ software (Version 1.50, National

Institutes of Health, Bethesda MD, USA).

5.5. Reagents and antibodies

LPS, IL-4 and all ELISA kits were obtained from R&D Systems (R&D Systems, USA). Cell culture reagents, including DMEM, Foetal bovine serum (FBS), antibiotics, trypsin–EDTA, PBS and other reagents were purchased from Thermo (Waltham, MA, USA). Monoclonal mouse anti-beta-actin (ab8226), polyclonal rabbit anti-iNOS (ab178945), anti-Liver Arginase (ab233548), anti-Mannose Receptor (ab64693), anti-NF-κB p65 (ab32536), anti-IκB alpha (ab32518), anti-phospho-IκB alpha (ab133462), anti-ERK (ab184699), anti-phospho-ERK (ab201015), anti-p38 (ab170099), anti-COX1 (ab109025), anti-RUNX2 (ab92336), anti-Osteopontin (ab63865), anti-TREM2 (ab305103), anti-DAP12 (ab283679), anti-ATG5 (ab108327), anti-ATG12 (ab303488), anti-ATG16L1 (ab188642), anti-STX17 (ab229646), anti-VAMP8 (ab76021), anti-SNAP29 (ab138500), anti-TNF alpha (ab1793), anti-CD31 (ab281583), anti-IL-6 (ab290735), and anti-TGF beta 1 (ab215715) were obtained from Abcam (Cambridge, MA). Polyclonal rabbit anti-Histones H3 (#4499), anti-Phospho-NF-κB p65 (#3033), anti-JNK (#9257), anti-Phospho-JNK (#9255) and anti-Phospho-p38 (#4511) were obtained from Cell Signaling (Danvers, MA, USA). Polyclonal rabbit anti-Osteocalcin (AB10911), anti-Beclin1 (SAB5700251), anti-SQSTM1 (SAB5700845), anti-LC3B (L7543), and anti-LAMP1 (SAB3500285) were obtained from Sigma Aldrich (St. Louis, MO, USA).

5.6. Cell viability assay

Each well was filled with CCK8 solution, and the samples were incubated for 2 h at 37 °C. To determine cell viability, the absorbance was measured at 450 nm using a microplate spectrophotometer (SpectraMax; Molecular Devices, Sunnyvale, CA). Three independent experiments were conducted in triplicate.

5.7. TREM2 small interfering RNAs (siRNAs), plasmids and cell transfection

Small interfering RNA (siRNA) oligonucleotides against TREM2 and the scrambled sequences were synthesized by Genomeditech Company (Shanghai, China). The sequences of the following siRNAs are listed in [Supplementary Table 1 A](#). According to the manufacturer's recommendation, use Lipofectamine 3000 (Invitrogen, USA) for transfection.

5.8. RNA isolation and real-time PCR

According to the manufacturer's instructions, total RNA was extracted from cells in each group using TRIzol reagent (Invitrogen, CA, USA). For each sample, use MLV reverse transcriptase to reverse transcribe 1 mg RNA according to the instructions. Use SYBR® Quantitative real-time PCR of specific transcripts by Premix DimerRaser™ (TaKaRa, Japan), and use RT-qPCR in ViiA for analysis™. The primers used for real time PCR are listed in [Supplementary Table 1 B](#).

5.9. ELISA

After the indicated treatment, macrophage medium was collected. The abundances of IL-1β, TNF-α, IL-6 and IL-1α were examined using mouse IL-1β (Abcam, ab197742), TNF-α (Abcam, ab208348), IL-6 (Abcam, ab222503) and IL-1α (Abcam, ab199076) ELISA kit in line with the guide of manufacturer. The outcomes are expressed in picograms per milliliter.

5.10. Immunofluorescence and image quantification

Fixed the cells with 4% PFA for 15 min, washed with PBS, and then broken with Triton $\times 100$ at room temperature for 20 min. After being washed again, the cells were incubated with closed buffer (PBS containing 10% goat serum and 1% BSA) for 1 h. Add antibody (1:400 dilution) and incubate at 4 °C overnight. After washing with TBS-T three times for 5 min, incubate goat anti-rabbit IgG antibody with 1:200 dilution conjugated with Alexa Fluor (Life Technologies, USA) in the dark at room temperature for 30 min. After washing in TBS-T solution, the nuclear DNA was stained with DAPI (Dojindo, Japan) for 5 min. Cover the petri dish with PBS and obtain the fluorescence microscope image (Olympus, Japan).

5.11. Nuclear and cytoplasmic extraction

After treatment, according to the instructions provided by the manufacturer, collect cells and use the nuclear extraction kit (Beyotime, China) to extract the nucleus and cytoplasmic protein, and determine the quality and purity of subcellular classification by using the immunoblotting of antibodies against the cytoplasm (β -actin) and cytoplasmic (Histones H3) protein.

5.12. Western blot analysis

After treatment, the cells were washed with cold PBS, and then ice-cold RIPA (Beyotime Biotechnology, Jiangsu, China) containing 10 mM phenylmethanesulfonyl fluoride (PMSF) was added and cracked on the ice for 30 min. Use the BCA assay kit (Beyotime Biotechnology, China) to determine the concentration of total cell protein. SDS-PAGE gel electrophoresis was used to separate and transfer the protein to polyvinylidene fluoride (PVDF) membrane. After the membrane was sealed in 5% skimmed milk dissolved in PBST buffer for 1 h, the membrane and the primary antibody were incubated overnight at 4 °C. After washing with TBS-T, the secondary antibody (1:5000, Abgent) conjugated with corresponding HRP was incubated at room temperature for 1 h. ECL kit (Pierce Chemical, Rockford, IL, USA) and Bio-Rad ChemDoc MP imaging system were used for chemiluminescence detection. Each experiment was conducted three times. Finally, the gray value of the band is analyzed by Image J software (National Institutes of Health).

5.13. Co-immunoprecipitation (Co-IP)

Resuspend cell particles in NP40 lysis buffer containing protease inhibitor, 14,000 \times G Centrifuge for 5 min. The supernatant was incubated overnight with the antibody of binding protein A + g magnetic beads at 4 °C. Before Western blot analysis, the beads were washed three times with lysis buffer.

5.14. *Staphylococcus aureus* infection and assessment of bacterial killing

S. aureus in the mid-log phase was diluted to 10^6 CFU/mL; 50 μ L of the bacteria suspension was added to 5.0 mL of LB broth containing AuNPs, and the mixture was incubated at 37 °C with gentle shaking. At predetermined intervals, 50 μ L of each suspension was spread on the agar plate, followed by a 24-h incubation at 37 °C. The number of visible colonies was determined, and the average CFU results were graphed against time on a log scale. Just before the cell infection, *Staphylococcus aureus* was evenly dispersed through a vortex oscillator and suspended in OD600 of 0.1 (about 1×10^8 CFU) in the infection medium (RPMI-1640, 10% FBS), diluted to reach the infection multiplicity (MOI) of 10:1, and then evenly dispersed again through the eddy current oscillator. Notably, 1.5×10^6 RAW264.7 cells were seeded into a 6-well plate well (Costar, Jiangsu, China). After treatment with AuNPs for 48 h, cells were infected

for 60 min with *S. aureus* in the early stationary phase. The extracellular bacteria were then eradicated by the addition of 200 μ g/mL gentamicin for 30 min at 37 °C, followed by the addition of fresh RPMI-1640 containing 10% FBS to the infected cells (0 hpi). The supernatants of infected cell cultures were removed and cells were lysed by the addition of 20 μ L of 0.1% Triton X-100. Extracellular bacteria were not removed. The supernatants were then combined with the lysates of the corresponding cells. Colonies were counted on plates containing dilutions yielding 30–300 visible colonies. The Live/Dead bacteria staining kit (Yeasen Biotechnology, Shanghai) was used to evaluate the cytotoxicity of bacterial survival in cell lysate after AuNPs treatments, as specified by the manufacturer.

5.15. Tandem mrfp-gfp-lc3 and GFP-LC3 fluorescence microscopy and measurement of lysosome distribution

To investigate autophagic flux, macrophages were transfected with an adenovirus expressing mRFP-GFP-LC3 (Genomeditech, China) for 48 h and then treated with AuNPs and infected with *S. aureus*. Macrophages were washed in PBS and incubated at 37 °C for 30 min with LysoTracker Deep Red (1/1000) and SYTO41 (1/500) to determine lysosome position. The cells were then photographed and analyzed using a confocal microscope (Olympus, Japan).

5.16. Experimental rat osteomyelitis and infectious skin defect model and treatment

Zoletil®50 was injected intramuscularly in accordance with 1 mL/kg body weight. After administering anesthesia, preparing the skin and disinfecting the thigh, a longitudinal incision was made on the anterolateral side of the rat femur to cut the skin, subcutaneous tissue, and deep fascia, exposing the femur along the space between the rectus femoris and the medial femoris. After drilling the femoral shaft with a 3 mm drill bit, the defect group was filled with a gel sponge saturated in deionized water. 1×10^8 cfu/mL bacterial liquid was injected into the infected group and 10 μ L was injected into the treatment group. The gelatin sponge was then filled (the gel sponge in the infection group was soaked in deionized water, whereas the gel sponge in the treatment group was soaked in AuNPs solution), and the wound was closed layer by layer with 3–0 suture. Following the operation, the mice are free to roam their cages. At the 2nd, 4th, and 6th week after surgery, 2 rats in each group were chosen for X-ray detection to observe the repair status of the femoral shaft defect. At the 6th week, all rats were killed and the materials were stored in 4% PFA.

After administering anesthesia, the skin on the back was prepared to create four 1 cm-diameter circular skin defects, with a distance of ≥ 1 cm between each defect. After suturing the bandage to the wound's surface, the defect group's wound is sutured with a bandage that absorbs sterile normal saline. The concentration of the drop solution for the wound of the infection group and the treatment group 1×10^8 cfu/mL bacterial liquid 100 μ L (The wound of the infection group was sutured with bandages that absorbed normal saline, and the wound of the treatment group was sutured with bandages that absorbed AuNPs solution). After the operation, the mice were free to move about their cage. One rat from each group was sacrificed 3, 7, and 14 days after surgery, and the skin tissue of the defect was photographed and preserved in 4% PFA.

This experiment was approved by the Research Ethics Committee of Shanghai General Hospital.

5.17. Histological analysis

The femur and skin were fixed with formalin solution for 48 h, the bone tissue was decalcified with disodium EDTA solution (12% v/v) for 28 days, dehydrated in ethanol, and embedded in paraffin. Consecutive

4 μm -thick horizontal sections were obtained from the defect area and then stained with H&E, Masson's trichrome and Safranin O staining for new bone and remnant scaffold assessment, and stained with Gram for evaluation of tissue infection, and imaged with inverted microscope (Olympus, Japan).

5.18. Immunohistochemical staining

Immunohistochemistry was carried out using a two-step detection kit (Zhongshan Golden Bridge Biotechnology, China). Briefly, specimens were immersed in antigen retrieval solution for 20 min, blocked for 30 min with 5% bovine serum albumin (BSA), and subsequently incubated with primary antibodies against mouse TNF- α (Abcam, ab1793) and IL-6 (Abcam, ab290735) for inflammatory cytokines markers, CD31 (Abcam, ab182981) and TGF- β (Abcam, ab215715) for promoting repair markers at 1:100 dilution overnight at 4 °C. After rinsing thoroughly in PBS, the horseradish peroxidase-conjugated secondary antibodies (Zhongshan Golden Bridge Biotechnology) were dropped onto slides. Each group is composed of more than three slides, and each slide was observed using a Zeiss light microscopy at the defect area including the scaffolds ($N > 3$).

5.19. Micro CT assessment

The rat osteomyelitis model femur was fixed for 24 h in 4% PFA. These were then analyzed using high-resolution μCT by the YUEBO Company (Hangzhou, China). Isotropic resolution was 6 μm . The femur was then reconstructed in three dimensions (3D).

5.20. RNA extraction, RNA-seq, and data analysis

TRIzol (Thermo Fisher Scientific) was used to extract total RNA from RAW264.7 cells, followed by lithium chloride precipitation for further purification. We sequenced RNA from nine samples derived from three matched groups of cells subjected to distinct treatments (Control group, *S. aureus* infection group, and AuNPs treated *S. aureus* infection group). Differentially expressed genes (DEG) were examined using weighted gene co-expression network analysis (WGCNA), Kyoto Encyclopedia of Genes and Genomes (KEGG) pathway analysis, and gene ontology (GO) enrichment analysis.

5.21. Statistical analysis

Student t-test was used to detect the difference between the two groups. All data were expressed as mean \pm SD of at least three independent experiments. Analysis of variance is used to detect differences among three or more groups. All statistical analyses were performed using SPSS version 18.0 software (IBM, Chicago, USA). (*) $P < 0.05$ was considered statistically significant.

Author statement

Wang Peilin: Conceptualization, Methodology, Validation, Formal analysis, Investigation, Data curation, Writing-original draft, Writing-review & editing, Visualization. Peng Ying: Validation, Formal analysis, Investigation, Writing-review & editing. Wang Renyuan: Methodology, Formal analysis, Writing-review & editing. Lin: Conceptualization, Formal analysis, Funding acquisition, Writing-review & editing. Lin Haodong: Conceptualization, Writing-review & editing, Visualization, Supervision, Project administration, Funding acquisition.

Declaration of competing interest

The authors declare that they have no known competing financial interests or personal relationships that could have appeared to influence the work reported in this paper.

Data availability

Data will be made available on request.

8. Acknowledgments

This work has been funded by Shanghai General Hospital (NO. 02.06.01.21.18) and Logistics Support Department of the Central Military Commission (NO. AWS18C001). The graphical abstract was created with BioRender.com and the agreement number of confirmation of publication and licensing rights was EP25A4LE7Q.

Appendix A. Supplementary data

Supplementary data to this article can be found online at <https://doi.org/10.1016/j.mtbio.2023.100700>.

References

- [1] J.E. Cassat, et al., A secreted bacterial protease tailors the *Staphylococcus aureus* virulence repertoire to modulate bone remodeling during osteomyelitis, *Cell Host Microbe* 13 (6) (2013) 759–772.
- [2] A. Nasser, et al., A comprehensive review of bacterial osteomyelitis with emphasis on *Staphylococcus aureus*, *Microb. Pathog.* 148 (2020), 104431.
- [3] S.S. Funk, L.A. Copley, Acute hematogenous osteomyelitis in children: pathogenesis, diagnosis, and treatment, *Orthop. Clin. N. Am.* 48 (2) (2017) 199–208.
- [4] Momodu II, V. Savaliya, *Osteomyelitis*, in *StatPearls*, StatPearls Publishing Copyright © 2022, StatPearls Publishing LLC, Treasure Island (FL), 2022.
- [5] T.J. Hatlen, L.G. Miller, *Staphylococcal skin and soft tissue infections*, *Infect. Dis. Clin.* 35 (1) (2021) 81–105.
- [6] M. Malone, G. Schultz, Challenges in the diagnosis and management of wound infection, *Br. J. Dermatol.* 187 (2) (2022) 159–166.
- [7] K.L. Urish, J.E. Cassat, *Staphylococcus aureus* osteomyelitis: bone, bugs, and surgery, *Infect. Immun.* 88 (7) (2020).
- [8] C. Zhong, et al., Advances in the antimicrobial treatment of osteomyelitis, *Compos. B Eng.* 249 (2023), 110428.
- [9] Wu, Y., et al., Peptide polymer-doped cement acting as an effective treatment of MRSA-infected chronic osteomyelitis. *Adv. Funct. Mater.* 32(7) 2107942, DOI10.1002/adfm.202107942.
- [10] T. Zheng, et al., YR/DFO@DCNT functionalized anisotropic micro/nano composite topography scaffolds for accelerating long-distance peripheral nerve regeneration, *Compos. B Eng.* 246 (2022), 110242.
- [11] M. Du, et al., Recent advances in biomedical engineering of nano-hydroxyapatite including dentistry, cancer treatment and bone repair, *Compos. B Eng.* 215 (2021), 108790.
- [12] J.A. Hubbell, S.N. Thomas, M.A. Swartz, Materials engineering for immunomodulation, *Nature* 462 (7272) (2009) 449–460.
- [13] E. Valsami-Jones, I. Lynch, NANOSAFETY. How safe are nanomaterials? *Science* 350 (6259) (2015) 388–389.
- [14] Y. Fan, et al., Construction of tissue-engineered vascular grafts with high patency by mimicking immune stealth and blocking TGF- β mediated endothelial-to-mesenchymal transition, *Compos. B Eng.* 251 (2023), 110487.
- [15] T. Hirai, et al., Metal nanoparticles in the presence of lipopolysaccharides trigger the onset of metal allergy in mice, *Nat. Nanotechnol.* 11 (9) (2016) 808–816.
- [16] J.Y. Ma, et al., Interactive effects of cerium oxide and diesel exhaust nanoparticles on inducing pulmonary fibrosis, *Toxicol. Appl. Pharmacol.* 278 (2) (2014) 135–147.
- [17] M.S. Goldberg, Immunoen지니어ing: how nanotechnology can enhance cancer immunotherapy, *Cell* 161 (2) (2015) 201–204.
- [18] J. Kim, et al., Injectable, spontaneously assembling, inorganic scaffolds modulate immune cells in vivo and increase vaccine efficacy, *Nat. Biotechnol.* 33 (1) (2015) 64–72.
- [19] N. Li, et al., Hybrid nanoparticles based on novel Schiff Base for durable flame retardant and antibacterial properties, *Compos. B Eng.* 238 (2022), 109905.
- [20] F. Rizzo, N.S. Kehr, Recent advances in injectable hydrogels for controlled and local drug delivery, *Adv. Healthc Mater.* 10 (1) (2021), e2001341.
- [21] Y. Li, et al., Biodegradable Mg-Cu alloy implants with antibacterial activity for the treatment of osteomyelitis: in vitro and in vivo evaluations, *Biomaterials* 106 (2016) 250–263.
- [22] J. Deng, et al., Advanced applications of cellulose-based composites in fighting bone diseases, *Compos. B Eng.* 245 (2022), 110221.
- [23] C. Shi, E.G. Pamer, Monocyte recruitment during infection and inflammation, *Nat. Rev. Immunol.* 11 (11) (2011) 762–774.
- [24] G. Weiss, U.E. Schaible, Macrophage defense mechanisms against intracellular bacteria, *Immunol. Rev.* 264 (1) (2015) 182–203.
- [25] S. Pérez, S. Rius-Pérez, Macrophage polarization and reprogramming in acute inflammation: a redox perspective, *Antioxidants* 11 (7) (2022).
- [26] L.A. Baxt, A.C. Garza-Mayers, M.B. Goldberg, Bacterial subversion of host innate immune pathways, *Science* 340 (6133) (2013) 697–701.

- [27] J. Huang, J.H. Brumell, Bacteria-autophagy interplay: a battle for survival, *Nat. Rev. Microbiol.* 12 (2) (2014) 101–114.
- [28] J. Cai, et al., Staphylococcus aureus facilitates its survival in bovine macrophages by blocking autophagic flux, *J. Cell Mol. Med.* 24 (6) (2020) 3460–3468.
- [29] M.I. Khan, et al., Induction of ROS, mitochondrial damage and autophagy in lung epithelial cancer cells by iron oxide nanoparticles, *Biomaterials* 33 (5) (2012) 1477–1488.
- [30] D. Huang, H. Zhou, J. Gao, Nanoparticles modulate autophagic effect in a dispersity-dependent manner, *Sci. Rep.* 5 (2015), 14361.
- [31] H. Li, et al., Alpha-alumina nanoparticles induce efficient autophagy-dependent cross-presentation and potent antitumour response, *Nat. Nanotechnol.* 6 (10) (2011) 645–650.
- [32] K. Peynshaert, et al., Exploiting intrinsic nanoparticle toxicity: the pros and cons of nanoparticle-induced autophagy in biomedical research, *Chem. Rev.* 114 (15) (2014) 7581–7609.
- [33] M. Li, et al., CCL5 deficiency promotes liver repair by improving inflammation resolution and liver regeneration through M2 macrophage polarization, *Cell. Mol. Immunol.* 17 (7) (2020) 753–764.
- [34] Y. Liu, et al., Attenuation of atherosclerosis by protocatechuic acid via inhibition of M1 and promotion of M2 macrophage polarization, *J. Agric. Food Chem.* 67 (3) (2019) 807–818.
- [35] S. Franz, et al., Overexpression of S100A9 in obesity impairs macrophage differentiation via TLR4-NFκB-signaling worsening inflammation and wound healing, *Theranostics* 12 (4) (2022) 1659–1682.
- [36] W. Chen, et al., Gold nanomaterial engineering for macrophage-mediated inflammation and tumor treatment, *Adv. Healthc Mater.* 10 (5) (2021), e2000818.
- [37] T.K. Prajsnar, et al., The autophagic response to Staphylococcus aureus provides an intracellular niche in neutrophils, *Autophagy* 17 (4) (2021) 888–902.
- [38] J.F. Gibson, et al., Neutrophils use selective autophagy receptor Sqstm1/p62 to target Staphylococcus aureus for degradation in vivo in zebrafish, *Autophagy* 17 (6) (2021) 1448–1457.
- [39] M. Wang, Z. Fan, H. Han, Autophagy in Staphylococcus aureus infection, *Front. Cell. Infect. Microbiol.* 11 (2021), 750222.
- [40] Y. Neumann, et al., Intracellular Staphylococcus aureus eludes selective autophagy by activating a host cell kinase, *Autophagy* 12 (11) (2016) 2069–2084.
- [41] M. Colonna, TREMs in the immune system and beyond, *Nat. Rev. Immunol.* 3 (6) (2003) 445–453.
- [42] Q. Chen, et al., Triggering receptor expressed on myeloid cells-2 protects against polymicrobial sepsis by enhancing bacterial clearance, *Am. J. Respir. Crit. Care Med.* 188 (2) (2013) 201–212.
- [43] S. Yang, et al., TREM2 dictates antibacterial defense and viability of bone marrow-derived macrophages during bacterial infection, *Am. J. Respir. Cell Mol. Biol.* 65 (2) (2021) 176–188.
- [44] Y. Wang, et al., TREM2/β-catenin attenuates NLRP3 inflammasome-mediated macrophage pyroptosis to promote bacterial clearance of pyogenic bacteria, *Cell Death Dis.* 13 (9) (2022) 771.
- [45] C. Zhou, et al., Recycling of autophagosomal components from autolysosomes by the recycler complex, *Nat. Cell Biol.* 24 (4) (2022) 497–512.
- [46] E. Itakura, C. Kishi-Itakura, N. Mizushima, The hairpin-type tail-anchored SNARE syntaxin 17 targets to autophagosomes for fusion with endosomes/lysosomes, *Cell* 151 (6) (2012) 1256–1269.
- [47] C. Viret, M. Faure, Regulation of syntaxin 17 during autophagosome maturation, *Trends Cell Biol.* 29 (1) (2019) 1–3.
- [48] W. Reizner, et al., A systematic review of animal models for Staphylococcus aureus osteomyelitis, *Eur. Cell. Mater.* 27 (2014) 196–212.
- [49] Y. Li, et al., An antibacterial bilayer hydrogel modified by tannic acid with oxidation resistance and adhesiveness to accelerate wound repair, *Colloids Surf. B Biointerfaces* 205 (2021), 111869.
- [50] Bz, A., et al., Injectable self-healing supramolecular hydrogels with conductivity and photo-thermal antibacterial activity to enhance complete skin regeneration. *Chem. Eng. J.* 400.
- [51] K. Chen, et al., Injectable melatonin-loaded carboxymethyl chitosan (CMCS)-based hydrogel accelerates wound healing by reducing inflammation and promoting angiogenesis and collagen deposition, *J. Mater. Sci. Technol. -Shenyang* 63 (2020).
- [52] S.K. Nandi, et al., Understanding osteomyelitis and its treatment through local drug delivery system, *Biotechnol. Adv.* 34 (8) (2016) 1305–1317.
- [53] J.C. Webb, R.F. Spencer, The role of polymethylmethacrylate bone cement in modern orthopaedic surgery, *J. Bone Joint Surg. Br.* 89 (7) (2007) 851–857.
- [54] L.L. Tundisi, et al., Nanotechnology as a tool to overcome macromolecules delivery issues, *Colloids Surf. B Biointerfaces* 222 (2022), 113043.
- [55] A. Curtis, C. Wilkinson, Nanotechniques and approaches in biotechnology, *Trends Biotechnol.* 19 (3) (2001) 97–101.
- [56] M. Zhu, et al., Cell-penetrating nanoparticles activate the inflammasome to enhance antibody production by targeting microtubule-associated protein 1-light chain 3 for degradation, *ACS Nano* 14 (3) (2020) 3703–3717.
- [57] D. Xu, et al., Tailorable hierarchical structures of biomimetic hydroxyapatite micro/nano particles promoting endocytosis and osteogenic differentiation of stem cells, *Biomater. Sci.* 8 (12) (2020) 3286–3300.
- [58] J. Penders, et al., Shape-dependent antibacterial effects of non-cytotoxic gold nanoparticles, *Int. J. Nanomed.* 12 (2017) 2457–2468.
- [59] T. Huang, et al., Engineering highly effective antimicrobial selenium nanoparticles through control of particle size, *Nanoscale* 11 (31) (2019) 14937–14951.
- [60] N.S. Mahmoud, et al., Role of nanoparticles in osteogenic differentiation of bone marrow mesenchymal stem cells, *Cytotechnology* 72 (1) (2020) 1–22.
- [61] W.K. Ko, et al., The effect of gold nanoparticle size on osteogenic differentiation of adipose-derived stem cells, *J. Colloid Interface Sci.* 438 (2015) 68–76.
- [62] J. Li, et al., Gold nanoparticle size and shape influence on osteogenesis of mesenchymal stem cells, *Nanoscale* 8 (15) (2016) 7992–8007.
- [63] X. Bai, et al., Bone formation recovery with gold nanoparticle-induced M2 macrophage polarization in mice, *Nanomedicine* 38 (2021), 102457.
- [64] X. Wu, et al., Au nanoclusters ameliorate Shigella infectious colitis by inducing oxidative stress, *Int. J. Nanomed.* 16 (2021) 4545–4557.
- [65] K. Zheng, et al., Antimicrobial gold nanoclusters, *ACS Nano* 11 (7) (2017) 6904–6910.
- [66] A. Rai, A. Prabhune, C.C. Perry, Antibiotic mediated synthesis of gold nanoparticles with potent antimicrobial activity and their application in antimicrobial coatings, *J. Mater. Chem.* 20 (32) (2010) 6789–6798.
- [67] V.D. Badwaik, et al., Size-dependent antimicrobial properties of sugar-encapsulated gold nanoparticles synthesized by a green method, *Nanoscale Res. Lett.* 7 (1) (2012) 623.
- [68] E.A. Ortiz-Benítez, et al., Antibacterial mechanism of gold nanoparticles on Streptococcus pneumoniae, *Metallomics* 11 (7) (2019) 1265–1276.
- [69] B. Lee, D.G. Lee, Synergistic antibacterial activity of gold nanoparticles caused by apoptosis-like death, *J. Appl. Microbiol.* 127 (3) (2019) 701–712.
- [70] M. Zhu, et al., TREM-2 promotes macrophage-mediated eradication of Pseudomonas aeruginosa via a PI3K/Akt pathway, *Scand. J. Immunol.* 79 (3) (2014) 187–196.
- [71] X. Xie, et al., Advanced glycation end products reduce macrophage-mediated killing of Staphylococcus aureus by ARL8 upregulation and inhibition of autolysosome formation, *Eur. J. Immunol.* 50 (8) (2020) 1174–1186.
- [72] Y.G. Zhao, P. Codogno, H. Zhang, Machinery, regulation and pathophysiological implications of autophagosome maturation, *Nat. Rev. Mol. Cell Biol.* 22 (11) (2021) 733–750.